

Title:

**A LINEAR ACOUSTIC MODEL FOR MULTI-CYLINDER I.C. ENGINE INTAKE  
MANIFOLDS INCLUDING THE EFFECTS OF THE INTAKE THROTTLE**

Authors:

**M.F. Harrison<sup>\*1</sup> and I. De Soto<sup>1,2</sup>, P.L. Rubio Unzueta<sup>1,3</sup>**

\* corresponding author

Professional addresses:

<sup>1</sup> School of Engineering,  
Cranfield University, Cranfield, Bedfordshire MK43 0AL, England

<sup>2</sup> Now at Ricardo MTC Ltd  
Southam Road, Radford Semele, Leamington Spa, Warwickshire CV31 1FQ, England

<sup>3</sup> Now at John Deere Iberica S.A.  
Crta.de Toledo km 12,200, 28905 Getafe. Madrid. Spain

Correspondence to:

Dr Matthew Harrison  
School of Engineering  
Whittle Building  
Cranfield University  
Cranfield  
Bedfordshire MK43 0AL

Reference: INTAKE MANIFOLD, Revision 2 (15<sup>th</sup> October 2003)

Total number of pages of text: 40 (including this page)

Total number of figures: 42

8038 words

**Abstract**

This paper presents a linear acoustic model of a multi-cylinder intake manifold that can be used as part of a hybrid time/frequency domain method to calculate the intake wave dynamics of practical naturally aspirated engines.

The method allows the user to construct a model of almost any manifold of complex geometry. The model is constructed as an assemblage of sub-models:

- (i) A model for a straight pipe with both ends open and through-flow.
- (ii) A model for an expansion chamber consisting of three lengths of pipe laid end-to-end: a narrow bore pipe expanding into a wide bore pipe contracting into a narrower bore pipe once more.
- (iii) A model of a side-branch, which includes a model for a straight pipe with one end closed and a model for the three way junction that joins the side-branch to a length of flow pipe.
- (iv) A model for an expansion with two (or more) side-branches, which combines the sub-models (i, ii, iii) into a multi-way (n-way) junction model.
- (v) A model for an intake throttle.

Good agreement with measurement has been found for each sub-model when bench-tested in isolation and encouraging agreement has been found when many sub-models are used together to model a complex intake manifold on a running engine.

## 1 Introduction

The intake manifold to an internal combustion (I.C.) engine will consist of a network of interconnecting pipes. The lengths of these pipes, and to a certain extent their diameters, must be chosen carefully as they will determine the resonant frequencies of the manifold. When the engine is run at a speed where one or more of these resonances is excited, then both the volumetric efficiency and the intake noise level may be affected.

This paper reports on part of an ongoing study of the acoustics of the intake manifold. To date, wave dynamics have been measured [1] and linear acoustic models have been developed to calculate this [2, 3] but only for single cylinder engines. This paper presents a linear acoustic model of a multi-cylinder intake manifold that can be used as part of a hybrid time/frequency domain method [4] to calculate the intake wave dynamics or practical naturally aspirated engines.

The method allows the user to construct a model of almost any manifold of complex geometry. The model is constructed as an assemblage of sub-models:

- (i) A model for a straight pipe with both ends open and through-flow.
- (ii) A model for an expansion chamber consisting of three lengths of pipe laid end-to-end: a narrow bore pipe expanding into a wide bore pipe contracting into a narrower bore pipe once more.

- (iii) A model of a side-branch, which includes a model for a straight pipe with one end closed and a model for the three way junction that joins the side-branch to a length of flow pipe.
- (iv) A model for an expansion with two (or more) side-branches, which combines the sub-models (i, ii, iii) into a multi-way (n-way) junction model.
- (v) A model for an intake throttle.

A similar modular approach has been adopted elsewhere for the construction of manifold models based on one-dimensional non-linear gas-dynamic theory. Benson et al [5] developed models for two types of three-way junction: the first where flow from one delivery pipe diverged into two collector pipes and the second where the flow from two delivery pipes converged into one collector pipe. In the latter case the pressure forces acting on the walls of the junction are known approximately and an appropriate momentum equation can be written and solved along with the conservation of mass and energy equations.

However, for the divergent flow case, these pressure forces are not known. Benson et al overcame this problem by measuring the pressure loss across such junctions during steady flow experiments and introducing empirical steady flow loss coefficients to their models. These empirical boundary conditions have been commonly used in I.C. engine simulation codes [6] being improved and extended in more recent times [7, 8].

The use of such empirical boundary conditions requires access to appropriate data for the flow loss coefficients. When this is not available a simplified constant pressure model must

be used [5]. This assumes that the pressure loss may be neglected and the flow may be assumed to be homentropic.

In the new manifold model presented in this paper, the effects of pressure loss in n-way pipe junctions are included. However, the linear acoustic model employed works on fluctuating components of pressure, density and particle velocity only. As a result, careful manipulation of the set of governing equations cancels the pressure loss term. This allows the solution of the acoustics of the manifold to be performed without the need for empirical loss coefficients. Simple empirical loss coefficients are subsequently used in the method but only to calculate the static pressure loss in the manifold. Therefore, if the user is only interested in the calculation of intake noise and not engine performance, the empirical loss coefficients are not needed.

In the present method steady state loss coefficients are not used in the calculation of any dynamic quantities whereas in the alternative gas dynamic methods [5, 6, 7, 8] they are. This can never be fully realistic particular at higher frequencies. Therefore, the present method represents an advance in modelling intake wave dynamics, particularly at higher frequencies. It is based on linear acoustic theory and remains applicable as long as dynamic pressure amplitudes remain sufficiently low. Investigations on the most extreme case, the Formula 1 racing engine [3], with dynamic pressures in the range of 0.8 bar, suggests that linear acoustic theory can be applied the intake of any naturally aspirated engine with some confidence.

## **2 Bench test cases for the linear plane wave acoustic sub-models**

The linear acoustic sub-models listed in the introduction were developed and tested against experiment [9,10]. A number of full size physical models were constructed using thick walled plastic pipe. These were tested using a particular form of wave-decomposition [1] using the experimental set-up shown in Figure 1. The tests were conducted without flow and using white noise excitation provided by a loudspeaker. The decision to test without flow was made in order to obtain the best possible signal-to-noise ratio for the wave decomposition without resorting to a more complex form of signal processing [11].

## **3 Overview of the linear plane wave acoustic models**

Five sub-models have been used. The first four of these are not new, being based on well-known models first reported around 1970 [12, 13]. However, they have never been tested together as an assembled model of a full intake manifold in the way that they have here. In addition, the influence of pressure loss on the construction of manifold models of this type has not been discussed before. Pressure loss is not an issue for the first model, (a straight open-open pipe), but it must be considered carefully in the four models that follow it and in the final assembled model of the full intake manifold.

The fifth sub-model, that for the intake throttle valve, is new.

### 3.1 Open-open straight pipe model

The particular straight pipe model employed here for the inflow boundary to an IC engine intake system has been used elsewhere [2, 3, 4].

The fundamental acoustic variables employed are fluctuating pressure  $p$ , fluctuating particle velocity  $u$  and fluctuating density  $\rho$ . These are related to the total pressure, velocity and density as follows:

$$p' = p_0 + p \quad (1)$$

$$u' = u_0 + u \quad (2)$$

$$\rho' = \rho_0 + \rho \quad (3)$$

where the subscript zero denotes stagnation conditions and the prime superscript denotes a total quantity.

The following useful relationships apply:

$$p = p^+ + p^- \quad (4)$$

$$\rho_0 c_0 u = p^+ - p^- \quad (5)$$

$$\rho = \frac{p^+ + p^-}{c_0^2} \quad (6)$$

The reference point of the model is a frequency varying acoustic reflection coefficient  $r$  [14] at the inflow end of the pipe (plane  $x=0$ ) which varies with inflow mean Mach number [15].

Appropriate end corrections apply and these also vary with Mach number [15].

$r_o$  gives the ratio of the amplitude of positive and negative travelling wave components  $p_o^+$  and  $p_o^-$  at plane  $x = 0$  thus:

$$r_o = \frac{p_o^-}{p_o^+} \quad (7)$$

An end correction of length  $l$  accounts for the phasing of  $p_o^+$  and  $p_o^-$ :

$$r = R_e^{i\theta} = - R_e^{i2kl} \quad \text{where } k \text{ is the wavenumber} \quad (8)$$

The wave components at any other plane ( $x$ ) in the pipe can be found using the following transformations:

$$p_x^+ = p_o^+ e^{i\beta(x+l)} \quad (9)$$

$$p_x^- = p_o^- e^{-i\beta(x+l)} \quad (10)$$

where  $\beta$  is a complex wavenumber taking Mach number and visco-thermal attenuation effects into consideration [16]

$$\beta = k + \alpha (1 - i) \quad (11)$$

and  $\alpha$  is a visco-thermal attenuation coefficient [16].

### 3.2 Expansion chamber model

The expansion chamber model used here has been derived elsewhere [13] with a detailed discussion of the physics of the problem given in [16]. The discussion here will concentrate on the effects of flow.

The expansion chamber is a common form of duct silencer and it consists of a sudden area expansion followed by a sudden area contraction as shown in Figure 2. The mass, momentum and energy conservation equations must be satisfied within a control volume that surrounds either geometrical discontinuity and these equations must be satisfied for both mean flow and acoustic fluctuations. In addition, the relevant boundary conditions must be satisfied. Figure 2 shows the two control volumes required to develop the expansion chamber model along with an indication of the expected flow shapes adapted from [16].

The sudden area contraction will be considered first as it is the simplest case. Measurements of the acoustic wavefront and of the flow velocity profile either side of the contraction show that both settle down very quickly after the contraction and resume their characteristic uniform shapes [13,16]. This suggests few physical irreversibilities in the contracting flow and, thus, the process may be assumed to be an isentropic process. Currie [17] shows rather neatly that for an adiabatic flow of an inviscid fluid where there are no body forces (i.e. adiabatic irreversible and isentropic flow) the stagnation enthalpy is constant along each streamline. That assumption is used to derive the non-conservative momentum equation down a streamline in isentropic flow:

$$c_o^2 = c^2 + \frac{\gamma - 1}{2} u^2 \quad (12)$$

where  $c$  is the sound speed,  $u$  is the velocity and  $\gamma$  is the ratio of specific heat capacities. Equation (12) is used in the formulation of many homentropic boundaries for gas-dynamic models of pipe inflow [4,6,7]. A fairly simple adiabatic boundary can be written in terms of Riemann variables [4] for the sudden area contraction without the need for empirical pressure loss coefficients.

The linear acoustic model of the sudden contraction is based on the simultaneous solution of the energy equation and the mass conservation equation, the momentum equation not being required as there are no losses.

As stagnation enthalpy per unit mass is conserved, the change in stagnation enthalpy can be written as:

$$dh_o = 0 \quad (13)$$

and differentiating (13)

$$dh + u \cdot du = 0 \quad (14)$$

Remembering that:

$$Tds = dh - \frac{dp}{\rho} \quad (15)$$

where  $s$  denotes specific entropy,  $p$  denotes pressure and  $\rho$  denotes density, on substitution:

$$Tds + \frac{dp}{\rho} + u \cdot du = 0 \quad (16)$$

Integrating with respect to mass across the large diameter duct (subscript 'J') and the narrower duct (subscript 'o'):

$$\left[ e + \frac{p'}{\rho'} + \frac{u^2}{2} \right]_{s_j} = \left[ e' + \frac{p'}{\rho'} + \frac{u^2}{2} \right]_{s_o} \quad (17)$$

where where e denotes specific internal energy

$$e = T_o ds \quad (18)$$

$$e' = e_o + e \quad (19)$$

Thus, energy is conserved across the junction in keeping with (17).

The equation of mass continuity for the sudden area contraction can be written:

$$\int_{s_j} \rho' u' dS_j = \int_{s_o} \rho' u' dS_o \quad (20)$$

The pair of equations (17, 20) can be written in terms of plane wave components  $p^+$ ,  $p^-$  [13, 16] and full derivations are given in [9]. So, subtracting the time average contribution, the energy equation for the fluctuating component at the contraction is:

$$\frac{1}{\rho_{0,J}} \left[ p_J^+ (1 + M_J) + p_J^- (1 - M_J) \right] = \frac{1}{\rho_{0,o}} \left[ p_o^+ (1 + M_o) + p_o^- (1 - M_o) \right] \quad (21)$$

where  $M$  is the Mach number.

The mass conservation equation describing the acoustic transfer at a contraction is:

$$\frac{S_J}{c_{0,J}} \left[ p_J^+ (1 + M_J) - p_J^- (1 - M_J) \right] = \frac{S_o}{c_{0,o}} \left[ p_o^+ (1 + M_o) - p_o^- (1 - M_o) \right] \quad (22)$$

Assuming  $\rho_{0,J} \approx \rho_{0,o}$  and  $c_{0,J} \approx c_{0,o}$  there is now a system of two equations (21,22) with two unknowns  $p_o^+$  and  $p_o^-$ , which can be found providing  $p_J^+$  and  $p_J^-$  are known as input obtained from an earlier calculation upstream of the contraction. For both (21) and (22) the outlet Mach number is given by

$$M_o = \frac{S_J}{S_o} M_J \quad (23)$$

as experimental evidence [16] suggests that the fully expanded flow within the control volume shown in Figure: 2b contracts down to the area of the outflow pipe with minimum losses.

The linear acoustic model for the sudden expansion is more complex. This is because flow separation at the expansion produces some areas of re-circulating flow (see Figure: 2a) and, hence, physical irreversibilities, and thus the expansion is non-isentropic.

This added complexity is dealt with in two steps. First conditions for an adiabatic expansion are calculated and then a correction to account for heat dissipation through viscosity, thermal conductivity or some other mechanism is added [13].

Assuming first an adiabatic expansion and hence no loss of  $h_o$ , from (17) and neglecting the time average terms and the products of two fluctuation properties, it can be written that:

$$\left[ T_o s + \frac{p}{\rho_o} + u_o u \right]_{s_i} = \left[ T_o s + \frac{p}{\rho_o} + u_o u \right]_{s_j} \quad (24)$$

where subscript 'I' denotes conditions in the narrower inlet pipe.

If there is some heat dissipation then entropy is no longer constant [12] and:

$$s = \frac{1}{e_o T_o} \phi \quad (25)$$

Where  $\phi$  is a complex function of viscosity and conduction.

Remembering the isentropic relationship

$$p = \rho c^2 \quad (26)$$

for the non-isentropic case the corrected form can be written [12]:

$$\rho = \frac{p + \delta}{c^2} \quad (27)$$

$$\delta = -(\gamma - 1) \varphi \quad (28)$$

There is little dissipation in the intake pipe so the acoustic energy conservation equation at an expansion (24) becomes:

$$\left[ \frac{p}{\rho_o} + u_o u \right]_{s_i} = \left[ T_o \left( \frac{1}{\rho_o T_o} \varnothing \right) + \frac{p}{\rho_o} + u_o u \right]_{s_j} \quad (29)$$

This energy equation can be written in terms of wave components, thus

$$\frac{1}{\rho_{o,i}} \left[ p_i^+ (1 + M_i) + p_i^- (1 - M_i) \right] = \frac{1}{\rho_{o,j}} \left[ p_j^+ (1 + M_j) + p_j^- (1 - M_j) - \frac{\delta}{\gamma - 1} \right] \quad (30)$$

Before the jet shown in Figure 2a is fully expanded, there are regions of recirculating flow. These areas do not make any contribution to the transport of acoustic energy and therefore it is reasonable to assume that  $M_j$  in equation (30) is equal to  $M_i$  providing the control volume is shorter than the length taken for the jet to fully expand. If the jet expands fully within the control volume then:

$$M_j = \frac{S_i}{S_j} M_i \quad (31)$$

The user of equation (30) is free to set  $M_j$  equal to  $M_i$  or to make use of the relationship given in equation (31). A rational choice should depend on the geometry of the expansion and that

of the downstream pipework. For most practical intake manifolds, an expansion is soon followed downstream by some other significant change in pipe cross sectional area, and it is unlikely that the jet will be fully expanded from the expansion before the flow changes shape once more. In such cases, it is sensible to declare a short control volume around the expansion and set  $M_J$  equal to  $M_I$ . For unusual intake manifolds that incorporate long plena, it might be preferable to declare a longer control volume to include the point at which the jet fully expands and to make use of equation (31).

The mass conservation equation is needed next followed by the momentum equation.

With plane wave propagation, the velocity  $u_w$  at the upstream wall of the expansion shown in Figure: 2a must be zero. In addition  $p_J^+$  and  $p_J^-$  at the downstream boundary of the control volume must match the values caused by the acoustic wave outside of the control volume. These two requirements can be satisfied either by introducing evanescent modes or by the use of an end-correction that acts as a protrusion of the inflow pipe beyond the upstream wall [16]. In the expansion model employed here,  $u_w$  is assumed to be zero and a phase correction term is added in the form of an end-correction to the length of the inlet pipe [13, 16].

The mass conservation equation can be written as:

$$\int_{S_I} (\rho_o u + u_o \rho) dS_I + \int_{S_w} (\rho_o u + u_o \rho_w) dS_w = \int_{S_J} (\rho_o u + u_o \rho) dS_J \quad (32)$$

The integral over  $S_w$  equals zero and from (22):

$$\int_{S_I} (\rho_o u + u_o \rho) dS_I = \frac{S_I}{c_{0,I}} [p_I^+ (1 + M_I) - p_I^- (1 - M_I)] \quad (33)$$

The integral over  $S_J$  needs close attention. From

$$u = \frac{p^+ - p^-}{\rho_o c_o} \quad (34)$$

It can be written that:

$$\int_{S_J} \rho_o u dS_J = S_J \left[ \frac{p_J^+ - p_J^-}{c_{0,J}} \right] \quad (35)$$

Re-circulating flow in the expansion is expected, so using (27)

$$\int_{S_J} u_o \rho dS_J = \int_{S_J} \left[ u_o \left( \frac{p + \delta}{c_o^2} \right) \right] dS_J \quad (36)$$

Using the simplified relationship:

$$u_{0,J} = u_{0,I} \left( \frac{S_I}{S_J} \right) \quad (37)$$

and the assumption  $c_{0,I} = c_{0,J}$ , the conservation of mass equation (32) becomes on substitution of (33), (35), (36) and (37).

$$S_I [p_I^+ (1 + M_I) - p_I^- (1 - M_I)] = S_J \left[ p_J^+ \left( 1 + \frac{S_I}{S_J} M_I \right) - p_J^- \left( 1 - \frac{S_I}{S_J} M_I \right) \right] + \delta S_I M_I \quad (38)$$

Although the regions of recirculating flow shown in Figure: 2a do not make any contribution to the transport of acoustic energy, they do contribute to the transport of mass. Recalling the discussion on control volume length for the energy equation (equation (30)), for the case of the mass conservation equation it seems more appropriate to, wherever geometry permits, set a control volume length that includes the point at which the flow jet becomes fully expanded and to declare:

$$M_J = \frac{S_I}{S_J} M_I \quad (39)$$

There are now two equations (30, 38) but three unknowns  $p_J^+$ ,  $p_J^-$  and  $\delta$  as  $p_I^+$  and  $p_I^-$  are inputs obtained from an upstream calculation. Rather than quantify  $\delta$  using experimental loss coefficients, the momentum equation is sought to provide a third equation and hence a solution to the three unknowns may be found.

Conservation of momentum across the expansion is expressed by equating the net flux of momentum to the axial pressure force:

$$\int_{S_J} \rho'_{S_J} (u'_J)^2 dS_J - \int_{S_I} \rho'_{S_I} (u'_I)^2 dS_I \approx \int_{S_I} p'_I dS_I + \int_{S_w} p'_w dS_w - \int_{S_J} p'_J dS_J \quad (40)$$

Noting the experimentally observed fact [16] that the stagnation pressure on the wall of the expansion ( $p_w$ ) equals the stagnation pressure in the outlet of the narrow upstream feed pipe

( $p_{0,J} = p_{0,I}$ ) and similarly the fact that the fluctuating pressure downstream of the expansion is observed to be almost radially uniform [16] the following approximate relationship holds:

$$\left(\rho'_J (u'_J)^2\right)S_J - \left(\rho'_I (u'_I)^2\right)S_I = p'_I S_I + p'_W S_W - p'_J S_J \quad (41)$$

Substituting (1, 3) expanding then neglecting the time average terms and the products of fluctuating terms:

$$\left(\rho_J u_{0,J}^2 + 2\rho_{0,J} u_{0,J} u_J\right)S_J - \left(\rho_I u_{0,I}^2 + 2\rho_{0,I} u_{0,I} u_I\right)S_I = p_I S_I + p_W S_W - p_J S_J \quad (42)$$

There are no flow losses in the inlet pipe so the second bracketed term may be expanded using (26) and (34).

$$\rho_I u_{0,I}^2 + 2\rho_{0,I} u_{0,I} u_I = \left(\frac{p_I^+ + p_I^-}{c_{0,I}^2}\right)M_I^2 c_{0,I}^2 + 2\rho_{0,I} M_I c_{0,I} \left(\frac{p_I^+ - p_I^-}{\rho_o c_{0,I}}\right) \quad (43)$$

There are flow losses in the junction and so (27) is used to expand  $\rho_J u_{0,J}^2$  in the first term, thus:

$$\rho_J u_{0,J}^2 + 2\rho_{0,J} u_{0,J} u_J = \left(\frac{p_J^+ + p_J^- + \delta}{c_{0,J}^2}\right)M_J^2 c_{0,J}^2 + 2\rho_{0,J} M_J c_{0,J} \left(\frac{p_J^+ - p_J^-}{\rho_{0,J} c_{0,J}}\right) \quad (44)$$

Substituting (43, 44) into (42) the conservation momentum equation for the fluctuating components is obtained:

$$\left[p_I^+ (1 + M_I (M_I + 2)) + p_I^- (1 + M_I (M_I - 2))\right]S_I + [p_W^+ + p_W^-]S_W = \left[p_J^+ M_J (M_J + 2) + p_J^- M_J (M_J - 2) + \delta M_J^2\right]S_J + [p_J^+ + p_J^-]S_J \quad (45)$$

The areas of recirculating flow shown on Figure: 2a do not make any contribution to the transport of fluctuating planar momentum. Recalling the discussion on control volume length for the energy equation (equation (30)), for the case of the momentum equation it seems appropriate to set a short control volume length and to declare that  $M_J$  in equation (45) is equal to  $M_I$ .

Both  $p_w^+$  and  $p_w^-$  appear in the conservation of momentum equation. These can be calculated from a sidebranch model where the length of the sidebranch is the length by which the inlet pipe protrudes into the expansion zone ( $d$ ) plus the appropriate end correction ( $e$ )

$$p_w^+ = \frac{(p_J^+ + p_J^-)}{1 + r_e} \quad (46)$$

$$p_w^- = r_e p_w^+ \quad (47)$$

$$r_e = \frac{1}{r_w} e^{i2\beta(d+e)} \quad (48)$$

The reflection at the wall is assumed to be near perfect and so  $r_w$  is given the value 0.99.

Equations (30, 38, 45) can be combined to eliminate  $\delta$  and to find  $p_J^+$  and  $p_J^-$  for a given input of  $p_I^+$  and  $p_I^-$ .

### 3.3 3-way junction with one open-closed pipe model

Figure 3 shows the general case. The pipe with the closed end is sometimes known as a “passive pipe” as there is wave action therein but no mean flow.

From the solution to the acoustic plane wave equation in one dimension it is known that [13]:

$$p(x, t) = p^+ e^{i(\omega t - \beta x)} + p^- e^{i(\omega t + \beta x)} \quad (49)$$

so it can be written that:

$$p_\ell^+ = p_o^+ e^{-i\beta \ell} \quad (50)$$

$$p_\ell^- = p_o^- e^{i\beta \ell} \quad (51)$$

If the boundary at  $x = 0$  is very rigid, say:

$$\frac{1}{r_{x=0}} = \frac{p_o^+}{p_o^-} = 0.99 \quad (52)$$

The reflection coefficient at  $x = \ell$  becomes:

$$r_p = \frac{p_1^-}{p_1^+} = \frac{p_o^- e^{i\beta \ell}}{0.97 p_o^- e^{-i\beta \ell}} = 1.01 e^{2i\beta \ell} \quad (53)$$

Assuming no flow losses across the passive pipe junction a continuity of pressure is declared so that:

$$p_{s_1}^+ + p_{s_1}^- = p_\ell^+ + p_\ell^- = p_o^+ + p_o^- = p_\ell^+ (1 + r_p) \quad (54)$$

If the input wave components are known  $(p_J^+, p_J^-)$  then  $p_\ell^+$  can be found, and, hence,  $p_\ell^-, p_o^+$  and  $p_o^-$ . The assumption of no flow losses across the passive pipe junction could usefully be examined by experiment in the future along with the well-known tendency for such junctions to cause flow noise.

### 3.4 The n-way junction model

The general case is shown in Figure 4. Assuming continuity of pressure in the junction:

$$p_J^+ + p_J^- = p_p^+ (1 + r_p) \quad (55)$$

$$\zeta_{p_1} = \frac{1 + r_{p_1}}{1 - r_{p_1}} \quad \text{and} \quad Z_{p_1} = \zeta_{p_1} \times S_1 \quad (56)$$

$$\zeta_{p_2} = \frac{1 + r_{p_2}}{1 - r_{p_2}} \quad \text{and} \quad Z_{p_2} = \zeta_{p_2} \times S_2 \quad (57)$$

Thus,

$$\zeta_p = \frac{1}{S_p} \left( \frac{S_1 \zeta_{p_1} S_2 \zeta_{p_2}}{S_1 \zeta_{p_1} + S_2 \zeta_{p_2}} \right) \quad (58)$$

assuming the impedances are in parallel and where  $S_1$ ,  $S_2$  and  $S_p$  are the cross sectional areas of the pipes concerned.

$$\zeta_p = \frac{1 + r_p}{1 - r_p} \quad (59)$$

$$r_p = \frac{\zeta_p - 1}{\zeta_p + 1} \quad (60)$$

Equation (53) can be solved for the n-way junction as for the case of the 3-way junction except (58) and (60) are also used to combine the impedances of the multiple passive pipes in parallel.

### 3.5 The intake throttle model

Both Benson and Blair have presented models for the throttle as part of complex gas dynamic and thermodynamic simulations of I.C. engine performance [6,18]. The models are different in some aspects of detail but they both treat the throttle as an adiabatic device where stagnation enthalpy is conserved but where there is also a pressure drop. Boundary conditions are imposed using Riemann variants where outgoing characteristic variables are influenced by the inclusion of empirical steady flow loss coefficients in the formulation of the boundary.

As the outgoing characteristic variables are affected, the value of loss coefficient employed affects the calculated wave action upstream and downstream of the throttle. Therefore, the Benson and Blair boundaries cause the throttle to produce both static pressure loss and altered wave action as is sometimes seen in practice with more highly tuned engines.

However, there is an apparent problem with such boundaries. Winterbone and Pearson [7] discuss the interaction between a simple wave and a device with an adiabatic pressure loss. The characteristics of the boundary model are such that the reflected wave amplitude  $p^+$  is

greater than the incident wave amplitude  $p^-$  and the transmitted wave amplitude is smaller than the incident wave amplitude. For steady flows this means a build up of pressure upstream of the device as would be expected. However, for oscillating flows or for steady flows with a superimposed sound field the boundary specifies a reflection coefficient that is greater than unity. This is not a realistic situation except at frequencies near to zero where mean flow momentum is converted to static pressure rise as the flow is arrested by the throttle. Therefore, although these boundaries do affect wave action, it is unlikely that this calculated effect will be realistic when the energy of the flow is stored at frequencies much above 0Hz.

The linear acoustic model for the throttle presented here does not suffer from this apparent problem. This is because the mean flow effects on static pressure distribution are calculated separately from the effects on wave dynamics. The static pressure losses are calculated using empirical loss coefficients [6].

The throttle model treats the partially open throttle as a finite length restriction in pipe area.

This finite restriction model is an assemblage of sub models:

- (i) In flow to a straight walled pipe of length  $L_2$  (referring to Figure: 5)
- (ii) Sudden contraction
- (iii) Straight pipe of length  $L_3$ , both ends open
- (iv) Sudden expansion
- (v) Straight pipe of length  $L_1$ , with both ends open

## 4 Results of the zero flow bench tests

The five sub-models described in Section 3 have been tested against zero flow bench tests as described in Section 2. Each test will be discussed in turn.

### 4.1 Testing the straight pipe model

The test case is shown in Figure 6. A loudspeaker was used to excite a 980mm long pipe with white noise. A two microphone wave decomposition technique [1] was used to measure the specific acoustic impedance ratio at plane 'i', in the duct. The two microphones used were Larson Davis type 2559 with Larson Davis type PRM200C pre-amplifiers and a Larson Davis microphone power supply type 2200C. The signals were recorded on a MDP500 dual channel minidisc recorder (a discussion of the consequences of this is given in [1]), digitised using an Iotech Daqbook 200 system and stored on a PC. All signal processing was performed using Matlab code written for the purpose [1].

Figure 7 shows the results from the straight pipe model with zero flow against experiment. The agreement between measured and calculated resonant frequencies (high  $\zeta$ ) is near perfect but the impedance levels at resonance vary. The extent of the variation is perhaps emphasised by the use of a linear impedance scale. The overall agreement is good.

## 4.2 Testing the expansion chamber model

The test case is shown in Figure 8. A comparison between measured and calculated results is shown in Figure 9. The agreement is generally very good.

## 4.3 Testing the 3-way junction model

The test case is shown in Figure 10. A comparison between measured and calculated results is shown in Figure 11. The agreement in resonant frequencies is good although the agreement in impedance level at resonance is restricted at low frequencies.

The impedance level is determined in part by the value of reflection coefficient modulus  $|r_p|$  employed to describe the closed end of the passive pipe. Figures 12, 13, 14 show the effect of reducing this from unity, through a value of 0.99 to a value to 0.95. A modified version of the wave decomposition technique [1] with four microphones has been used to measure the attenuation (dB) afforded by the passive pipe.

$$\text{ATT}(\text{dB}) = \frac{p_o^+}{p_i^+} \quad (61)$$

Reducing  $|r_p|$  reduces the amplitude of the attenuation at anti-resonance to be nearer the value found by experiment but it has the side-effect of deepening the dip in attenuation caused at a slightly lower frequency. A value for  $|r_p|$  of 0.99 seems a reasonable compromise and this value has been used throughout the work reported here.

#### 4.4 Testing the n-way junction model

The test case is shown in Figure 15. A comparison between measured and calculated results is shown in Figure 16. The agreement is fairly good. The full model has been constructed by bringing models for the straight outlet pipe, the contraction, the passive 3-way junction and the expansion together.

#### 4.5 Testing the intake throttle model

The test case is shown in Figure: 17. The reflection coefficient 700 mm downstream of the throttle was measured with the throttle removed, with it wide open, with it fully closed, and at several settings with it partially open. Figures: 18, 19, 20 show the measured impedance ratio for the fully open, fully closed and 5 degrees open cases respectively. The suppression in standing wave ratio is seen as a lower peak in impedance at resonance, around  $9.5 \rho_o c_o$  with 5 degrees opening, compared with  $15 \rho_o c_o$  for wide open throttle and  $>20 \rho_o c_o$  for the fully closed throttle.

Figure:21 shows the impedance spectra measured at several throttle positions. With the throttle more than  $5^\circ$  open, the resonant and anti resonant frequencies are hardly affected by a change in throttle angle.

The throttle geometry is shown in Figure: 22. The radius  $R_2$  of the restriction of length  $L_3$  is given by:

$$R_2 = R_1 \sqrt{1 - \cos \alpha} \quad (62)$$

The average physical length  $L_E$  can be calculated thus:

$$L_E = 0.635 \times 2R_1 \sin \alpha \quad (63)$$

as shown in Table: 1 and where the factor 0.635 is the mean value for the distance between the edge of the throttle blade and the throttle spindle (see Figure: 22). The appropriate length of the restriction is found by trial and error so that calculated results best match those from experiment.

$\alpha$	$R_2$	$L_E$
90	19	24.1
67.5	14.9	22.3
45	10.3	17.1
30	7.0	12.6
15	3.5	6.2
5	1.2	2.1
0	0	0

Table 1 intake throttle geometry

Figures: 23, 24, 25 show measured and calculated results for the 45° throttle with  $R_2 = 10.3\text{mm}$  and the acoustic length of the restriction being set to 1 mm, 5.5 mm and 10 mm respectively. It is clear that the resonant frequencies match best when the acoustic length is set to 5.5 mm which is 32% of the averaged physical length  $L_E$  shown in Table: 1. Figures: 26, 27, 28 show matches for resonant frequencies for 30°, 15°, 5° openings respectively and in each case the acoustic length used was 25%, 21% and 33% of the averaged physical length respectively.

So, the finite length restriction model predicts resonant frequencies correctly providing that the acoustic length of the restriction is some 20-30% on average of the physical equivalent length calculated using (63). The model does not however predict the suppression of standing wave ratio with closing throttle that was found in the experiments.

## 5 Case study on a running four-cylinder engine

The five linear plane wave acoustic sub-models described in Section 3 have been tested on a bench as reported in Section 4. Such tests provide the best possible conditions for the wave-decomposition measurements and thus there is good confidence in the measured results for specific acoustic impedance ratio. Such confidence is necessary when de-bugging the computer code used to generate the modelling results.

Notwithstanding this, it remains necessary to determine how useful the acoustic models prove to be when applied to a real test case.

Wave decomposition measurements have been made on the intake system of a 1.0 litre, four-cylinder, four-stroke gasoline engine that is currently fitted to a small mass-produced car. The engine was run on a dynamometer in a large open-plan laboratory as shown in Figure: 29, with the exhaust gases piped away to the outside of the building.

An experimental end feed intake manifold was manufactured for the tests (Figure: 30). The manifold assembly consisted of four parts; an intake pipe, a throttle body, a plenum with four pipes (known as ‘runners’) leading to the intake ports, and a holder for the four fuel injectors fitted to the engine. The manifold dimensions were representative of a typical end-feed system designed to boost lower speed torque and are shown in Figure: 31.

Each runner was drilled and tapped in three locations, two opposite each other at a distance of 100mm from the junction with the plenum and one at 250mm from that junction (see Figure:

31). Two Kistler type 4045A2 (2 bar) piezo-resistive pressure transducers were used to measure of both static and dynamic pressures at these tappings. Their signals were amplified using two Kistler type 4611 amplifiers and the resulting fluctuating voltages were digitised using a 16-bit National Instruments acquisition system and stored on a PC. The digitised signals were post processed off-line using codes written in Matlab™.

Many engine tests were performed. The speed-control mode of the dynamometer was used to set the engine to speeds in the range  $1200\text{-}3200\text{ revmin}^{-1}$  in steps of  $200\text{ revmin}^{-1}$ . Long sequences of intake pressure data (25 seconds, acquired at 8192 Hz) were acquired simultaneously in each case. For the first tests, pressures were measured at the two tappings that are opposite to one another in runner 1 and the results used for the calibration part of the wave-decomposition technique [1]. Other tests were made with the two transducers 150mm apart. These later tests were repeated for each of the four runners. The engine was operated first with a wide-open throttle and then with the throttle partially closed (15% open, as measured using the throttle position sensor on the engine). A total of 176 tests were performed along with 22 calibrations.

Figure: 32 shows the torque output of the engine as measured by the dynamometer with the engine running first with a wide-open throttle and then with a throttle that is 15% open. A peak in the wide-open throttle torque curve is clearly seen at  $2000\text{ revmin}^{-1}$ . The shape of the part load torque curve is due to the ignition maps used with the engine. At the lowest speeds, the ignition timing is 10 degrees before top dead centre for both wide-open and part throttles. At higher speeds, the ignition is advanced for the wide-open throttle case but retarded for the part throttle case. The retarding of the part-throttle ignition timing is a deliberate strategy to promote rapid deceleration of the engine when the throttle is suddenly released at high engine

speeds. It is accompanied by an increase in fuel-air ratio to preserve the life of the catalytic converter.

Figure: 33 shows the fluctuating component of pressure measured in each of the four runners with the engine at the peak torque condition ( $2000 \text{ revmin}^{-1}$ , wide-open throttle). The pressure signals are near sinusoidal, with high amplitude and little variation between those measured in different runners. This pattern is in marked contrast to that found in single cylinder engines [1, 3] where the intake pressure signal consists of a pressure depression as the intake valve opens, followed by a pressure peak as the valve closes, followed by a decaying oscillation before the valve starts to open once more. The pattern in Figure: 33 is easily explained. The pressure peaks recorded in runner 1 occur every 0.25 of a four-stroke cycle. Each one originates from a different intake stroke (there being four per cycle in this four-cylinder engine) and will be caused by the period when the respective intake valve is open. At this particular operating condition, when the intake pressure is at a maximum in runner 1 it is also near to a maximum in the other runners. The mode of behaviour for the wave action is therefore clearly well organised (i.e. resonant) as the pressure waves in each runner are synchronous with each other. The fluid motion can be visualised as a synchronous sloshing up and down the four runners. Resonant behaviour in the intake system would be expected at this operating condition as the torque is at a maximum [3]. The average distance between the intake ports of the four cylinders is 660mm (taken along the centreline of the runners and plenum), which at a sound speed of  $343 \text{ ms}^{-1}$  would be covered in 1.9 ms or 0.032 of the time taken to complete one four-stroke cycle at  $2000 \text{ revmin}^{-1}$ . This phase delay of 0.032 cycles is small compared with the interval between pressure peaks which is 0.25 cycles and so the time interval between peaks is (almost) uniform.

Figure: 34 shows the fluctuating component of pressure measured in each of the four runners with the engine at a low torque condition ( $1400 \text{ revmin}^{-1}$ , wide-open throttle). This time the pressure amplitude is much smaller than for the peak torque condition (1/3 of the amplitude) although the torque has only dropped by 20%. The wave action in the intake manifold is not well organised as the pressure peaks in runner 1 do not occur at the same time as those in the other runners. The pressure peaks in the other runners are in phase with each other however, suggesting resonant behaviour in only part of the manifold at this operating condition.

Figure: 35 shows the fluctuating component of pressure measured in each of the four runners with the engine at an intermediate torque condition ( $2400 \text{ revmin}^{-1}$ , wide-open throttle). This time the pressure amplitude lies between the amplitudes noted for the high and low torque operating conditions (Figures: 33, 34 respectively) and the wave action is not well organised in any part of the manifold.

Figure: 36 shows the fluctuating component of pressure measured in each of the four runners with the engine at a  $2000 \text{ revmin}^{-1}$ , 15% open throttle. The influence of part throttle operation on the intake pressures is clearly seen when Figure: 36 is compared with Figure: 33. The part throttle attenuates the pressure amplitude, distorts the waveform, disrupts the well-organised wave motion in the manifold and introduces higher frequency noise to the waveform. These effects are also seen in the respective spectra for the two pressure signals (Figures: 37, 38). The spectra are the average of more than one hundred 2048 point FFTs in each case, producing a spectral resolution of 4 Hz. The tonal quality of the pressure signal for the wide-open throttle case is clearly seen in Figure: 37.

Figure: 39 shows the coherence obtained between two pressure signals recorded 150mm apart in runner 1 of the engine,  $2400 \text{ revmin}^{-1}$ , wide-open throttle. The coherence is good only at low frequencies where the sound pressure level has a tonal peak. Figure: 40 shows the corresponding result at  $2400 \text{ revmin}^{-1}$ , 15% open throttle. The higher frequency coherence is improved due to the more evenly distributed spectral shape found with the part-throttle results when compared with the wide-open throttle results (Figure: 38 compared with 37).

Overall, the coherence between pressure signals measured in the same intake runner is poor compared to what has been achieved before on a running single-cylinder engine [1]. Therefore, a particular adaptation of the regular wave-decomposition technique was employed here to mitigate against this problem. The wave-decomposition calculation was performed in the usual way [1] but the results were then post-processed. The results at any frequency were discarded unless the coherence between the two pressure signals was greater than 0.99. As a result, for every engine speed and load condition, wave decomposition results were only obtained at between 5 and 20 of the 1024 spectral lines available. However, when the results from all the speeds are combined, a rather sparse composite picture of the specific acoustic impedance ratio is obtained, where the few results that are shown are deemed to be reliable. This composite picture is rather unusual because the results have been obtained with a wide range of volume flow rates through each runner. The volumetric efficiency of the engine was known and hence the volumetric flow rates could be found for each speed and the correct time-averaged flow rate was used for each wave-decomposition experiment.

Figure: 41 shows the composite results obtained for the speed range  $1200\text{-}3200 \text{ revmin}^{-1}$  with a wide-open throttle and Figure: 42 shows the corresponding results for a throttle that is only 15% open. The results obtained from a linear acoustic model of the full intake system (including the throttle) assembled using the 5 sub-models described in Section 3 are also

shown. In each case, a single speed-averaged volumetric flow rate has been used in the modelling, assuming that the flow is evenly distributed across all four runners. The modelling is undertaken separately for each runner and it is assumed that only the runner being modelled has flow and that the valves that terminate the other runners remain shut. However, the measurements are made over many complete cycles and therefore wave action is recorded in runners that have valves that open and close (and hence provide time-varying flow rates). Therefore, the modelling is a simplification of the true behaviour with respect to the flow in the manifold and to the time-varying termination impedance of each runner (high when the valve is closed, lower when it is open).

A number of observations can be made regarding the measured data shown in Figures: 41, 42.

Firstly, the measured spectral shape of the specific acoustic impedance ratio shown in Figure: 41 is different in each runner, although the results for runners 2 and 3 are quite similar. All four show a peak at the same low frequency. This feature is responsible for the resonant behaviour noted at  $2000 \text{ revmin}^{-1}$  in Figure: 33.

Secondly, by comparing Figures: 41 and 42, it can be seen that the spectral shape of the measured specific acoustic impedance ratio changed significantly with throttle angle. Note the loss of the low frequency peak when the throttle valve is partially closed, echoing the disruption to resonant behaviour noted in Figure: 36

Thirdly, the magnitude of the measured specific acoustic impedance ratio is quite low (mostly below  $10 \rho_0 c_0$ ) and therefore resonant wave action in the manifold will be weaker than

might otherwise be expected from the calculated results. The width of the peaks in the measured specific acoustic impedance ratio suggests the presence of some effective mechanism of wave-damping. This might be due to either flow separation or the effects of pulsile flow or flow induced noise.

Finally, the acoustic characteristics of runner 4 as shown in Figure: 42 are unusual as a strong peak in the measured results is shown at 250 Hz. This is not seen in the results for runners 2,3 and seen only weakly in the results for runner 1. Runner 4 is very near the throttle body so it experiences a different flow field to the other three runners and this may explain the unusual behaviour.

The results from the modelling are encouraging. Notwithstanding the difficulties in obtaining reliable measured results, the results that are shown do correspond quite closely to the results from the model at the lower frequencies. The modelling produces very different results for each runner and for different throttle settings, justifying the level of detail adopted. Given the unsteady nature of the flow in such a manifold, the relative simplicity of the modelling and the possibilities for flow induced noise, the validation is thought to be good.

## **6 Conclusions**

A calculation method has been developed and tested against experiment that allows the user to construct an acoustic model of a complex I.C. engine intake manifold from an assemblage of sub-models.

Good agreement with measurement has been found for each sub-model when bench-tested in isolation and encouraging agreement has been found when many sub-models are used together to model a complex intake manifold on a running engine.

## **Acknowledgements**

The first author gratefully acknowledges the support of EPSRC for this work, made possible under grant no: GR/RO4324.

## References

- 1 M.F. Harrison & P.T. Stanev, 2003, Journal of Sound and Vibration (in press), Measuring wave dynamics in IC engine intake systems.
- 2 M.F. Harrison & P.T. Stanev, 2003, Journal of Sound and Vibration (in press), A linear acoustic model for intake wave dynamics in IC engines.
- 3 M.F. Harrison & A. Dunkley, 2003, Journal of Sound and Vibration (in press), The acoustics of racing engine intake systems.
- 4 M.F. Harrison & R. Perez Arenas, 2003, Journal of Sound and Vibration (in press), A hybrid boundary for the prediction of intake wave dynamics in IC engines.
- 5 R.S. Benson, D. Woollatt & W.A. Woods, 1963-1964, Process, Instrumentation and Mechanical Engineers, Vol. 179, Part 3, p24-49, Unsteady flow in simple branch systems.
- 6 R.S. Benson, 1982, Clarendon Press, Oxford, The thermodynamics and gas dynamics of internal combustion engines – Vol. 1.
- 7 D.E. Winterbone & R.J. Pearson, 2000, Professional Engineering Publishing Ltd, London, Theory of engine manifold design: wave action methods for IC engines.

- 8 J.F. Bingham & G.P. Blair, 1985, Proceedings of I.Mech.E, Vol. 199, An improved branched pipe model for multi-cylinder automotive engine calculations.
- 9 I. De Soto Boedo, 2001, MSc Thesis, Cranfield University, The acoustics of internal combustion engine manifolds.
- 10 P.L. Rubio Unzueta, 2001, MSc Thesis, Cranfield University, Quantifying throttle losses.
- 11 K.R. Holland & P.O.A.L. Davies, 2000, Journal of Sound and Vibration, 230(4), 915-932, The measurement of sound power flux in flow ducts.
- 12 Mungur, Gladwell, 1969, Journal of Sound and Vibration, 9, 28-48, Acoustic wave propagation in a sheared fluid contained in a duct.
- 13 R.J. Alfredson & P.O.A.L. Davies, 1971, Journal of Sound and Vibration, 15, pp175-196, Performance of exhaust silencer components.
- 14 P.O.A.L. Davies, J.L. Bento Coelho & M. Bhattacharya, 1980, Journal of Sound and Vibration, 72(4), pp543-546, Reflection coefficients for an unflanged pipe with flow.
- 15 P.O.A.L. Davies, 1987, Journal of Sound and Vibration, 115(3), pp560-564, Plane wave reflection at flow intakes.

- 16 P.O.A.L. Davies, 1988, Journal of Sound and Vibration, 124(1), pp91-115, Practical flow duct acoustics.
- 17 I.G. Currie, 1993, McGraw Hill, New York, Fundamental mechanics of fluids – 2<sup>nd</sup> edition.
- 18 G.P. Blair, 1999, Society of Automotive Engineers, Warrendale Pa., Design and simulation of 4-stroke engines.

## Figure labels

- Figure: 1      Experimental setup.
- Figure: 2      Control volumes used to develop sub models for sudden expansion and contraction in area. Adapted from [16].
- Figure: 3      Sub model for a three way junction with a passive pipe.
- Figure: 4      Sub model for the n-way junction
- Figure: 5      Throttle simulation sub-model.
- Figure: 6      Sketch of the dimensions of the pipe and the position of the microphones and the loudspeaker
- Figure: 7      Measured (solid line) and calculated (dashed line) specific acoustic impedance ratio for a straight pipe.
- Figure: 8      Simple expansion chamber tested.
- Figure: 9      Measured (solid line) and calculated (dashed line) specific acoustic impedance ratio for the simple expansion chamber.
- Figure: 10     Submodel for the passive pipe.

Figure: 11 Measured (solid line) and calculated (dashed line) specific acoustic impedance ratio for the passive pipe.

Figure: 12 Passive pipe attenuation. Measured and calculated with  $r=1$ . Measured (solid line) calculated (dashed line).

Figure: 13 Passive pipe attenuation. Measured and calculated with  $r=0.99$ . Measured (solid line) calculated (dashed line).

Figure: 14 Passive pipe attenuation. Measured and calculated with  $r=0.95$ . Measured (solid line) calculated (dashed line).

Figure: 15 Submodel for the n-way junction.

Figure: 16 Measured (solid line) and calculated (dashed line) specific acoustic impedance ratio for the n-way junction.

Figure: 17 Throttled pipe test piece. Dimensions in millimetres.

Figure: 18 Wide open throttle measurement of specific acoustic impedance ratio.

Figure: 19 Fully closed throttle measurement of specific acoustic impedance ratio.

Figure: 20  $5^\circ$  open throttle measurement of specific acoustic impedance ratio.

- Figure: 21 Measured partial throttle results. Throttle angles in the range 5-90 degrees.  
Closed throttle (dashed line).
- Figure: 22 Geometry to consider when calculating effective length of the throttle valve.
- Figure: 23 Measured (solid line) and calculated (dashed line) results for 45° open throttle,  
L3=1mm.
- Figure: 24 Measured (solid line) and calculated (dashed line) results for 45° open throttle,  
L3=5.5mm.
- Figure: 25 Measured (solid line) and calculated (dashed line) results for 45° open throttle,  
L3=10mm.
- Figure: 26 Measured (solid line) and calculated (dashed line) results for 30° open throttle,  
L3=3mm.
- Figure: 27 Measured (solid line) and calculated (dashed line) results for 15° open throttle,  
L3=1.3mm.
- Figure: 28 Measured (solid line) and calculated (dashed line) results for 5° open throttle,  
L3=0.7mm.
- Figure: 29 Photograph of the engine.

Figure: 30 Photograph of the experimental intake manifold. The throttle body and intake pipe are not shown.

Figure: 31 Manifold dimensions in millimetres.

Figure: 32 Torque output of the engine. wide-open throttle (solid line), 15% open throttle (dashed line).

Figure: 33 Acoustic pressures in each of the four runners, 2000 revmin<sup>-1</sup> wide-open throttle. Runner 1 (solid line), runner 2 (dashed line), runner 3 (heavy dotted line), runner 4 (chain dot line).

Figure: 34 Acoustic pressures in each of the four runners, 1400 revmin<sup>-1</sup> wide-open throttle. Runner 1 (solid line), runner 2 (dashed line), runner 3 (heavy dotted line), runner 4 (chain dot line).

Figure: 35 Acoustic pressures in each of the four runners, 2400 revmin<sup>-1</sup> wide-open throttle. Runner 1 (solid line), runner 2 (dashed line), runner 3 (heavy dotted line), runner 4 (chain dot line).

Figure: 36 Acoustic pressures in each of the four runners, 2000 revmin<sup>-1</sup> 15% open throttle. Runner 1 (solid line), runner 2 (dashed line), runner 3 (heavy dotted line), runner 4 (chain dot line).

Figure: 37 Pressure spectrum in runner 1 obtained at  $2000 \text{ revmin}^{-1}$  wide-open throttle.

Figure: 38 Pressure spectrum in runner 1 obtained at  $2000 \text{ revmin}^{-1}$  15% open throttle.

Figure: 39 Coherence between two pressure measurements made in runner 1 at  $2000 \text{ revmin}^{-1}$  wide-open throttle.

Figure: 40 Coherence between two pressure measurements made in runner 1 at  $2000 \text{ revmin}^{-1}$  15% open throttle.

Figure: 41 Wide-open throttle results. Measured results (crosses), calculated (solid line).

Figure: 42 15% open throttle results. Measured results (crosses), calculated (solid line).

Harrison, De Soto, Rubio Unzueta – Figures

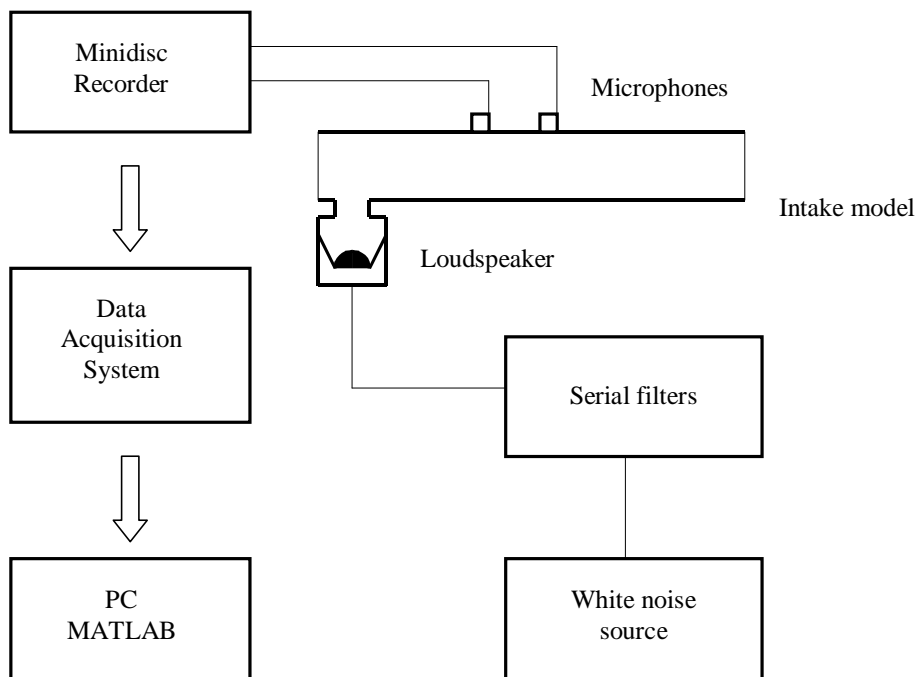


Figure: 1

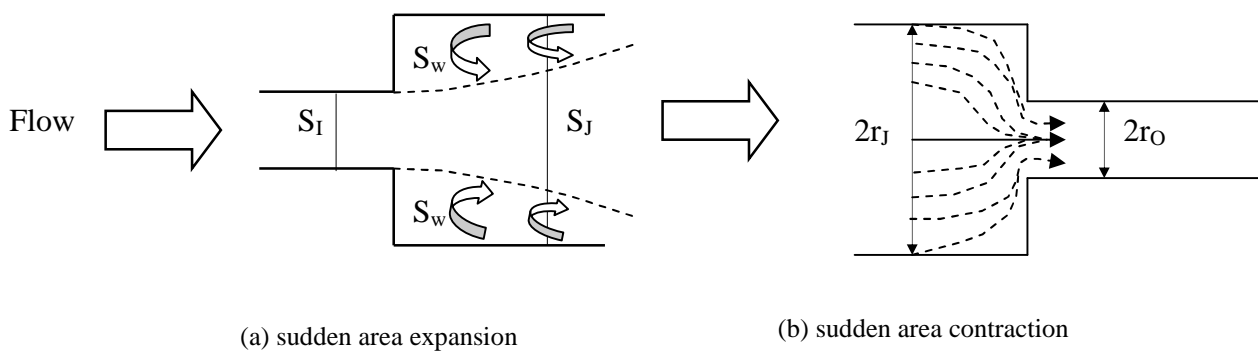


Figure: 2

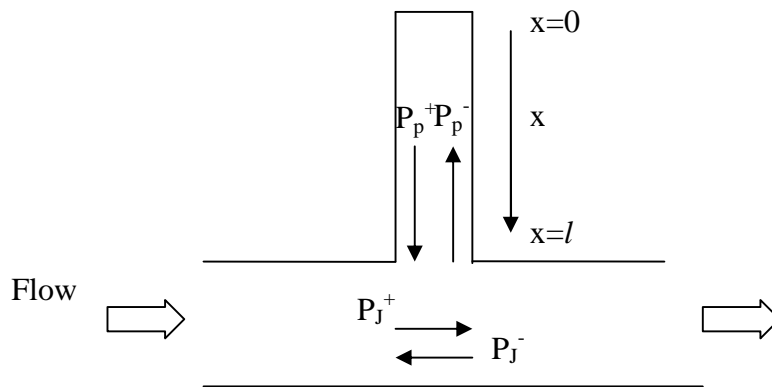


Figure: 3

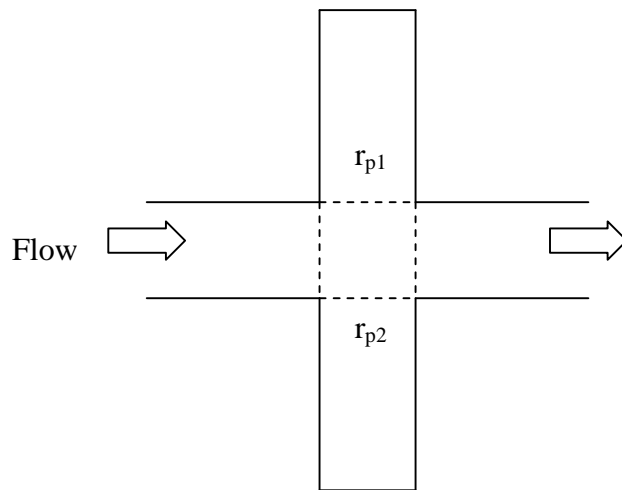


Figure: 4

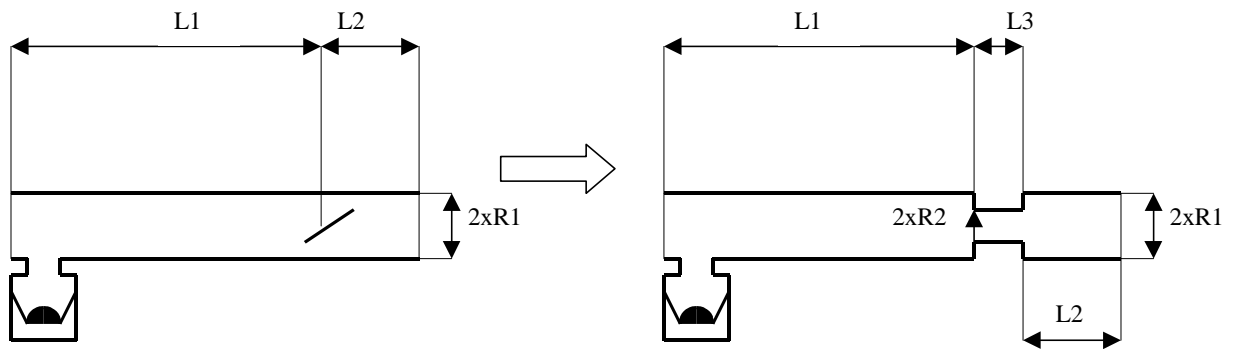


Figure: 5

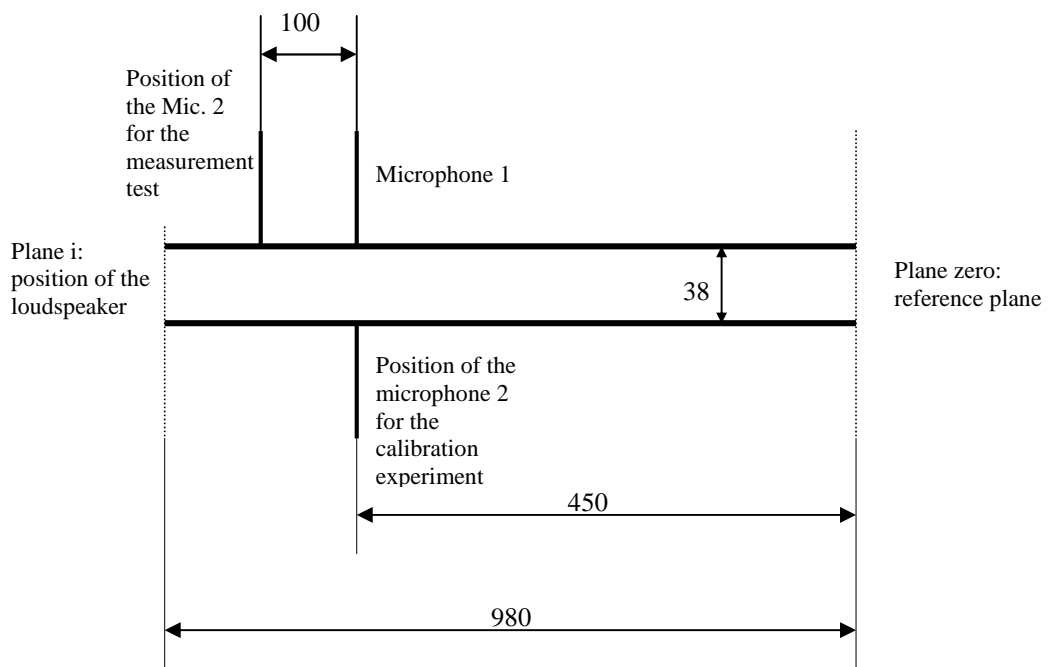


Figure: 6

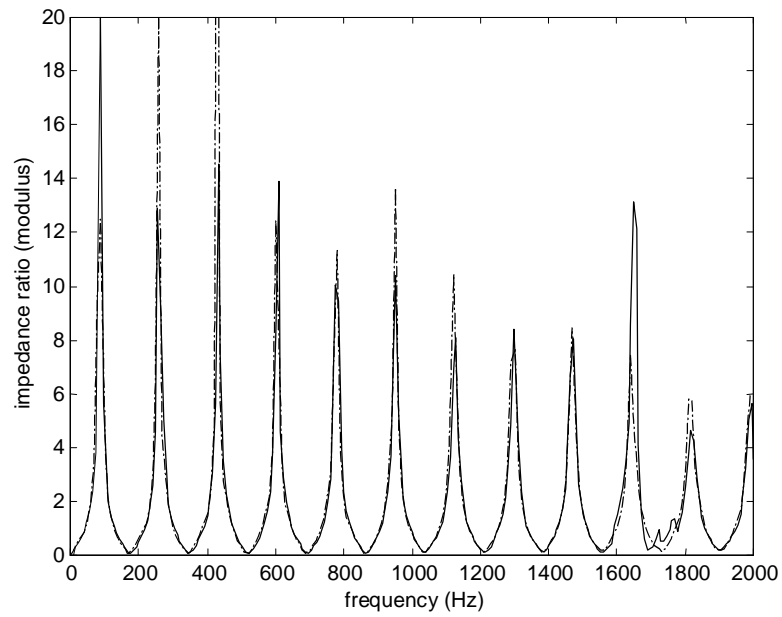


Figure: 7

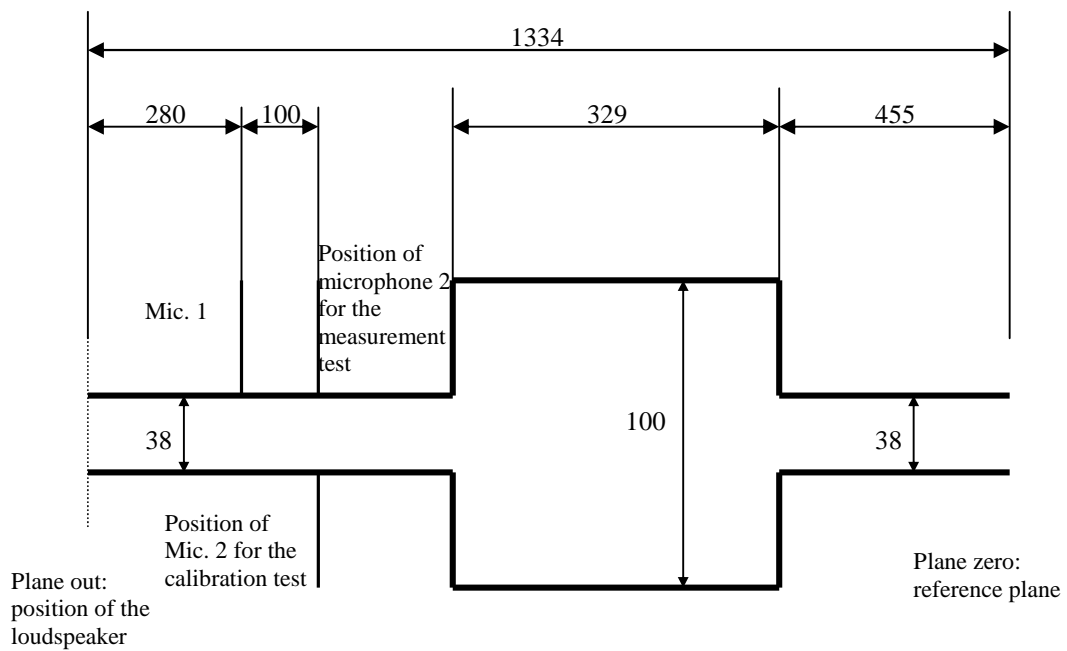


Figure: 8

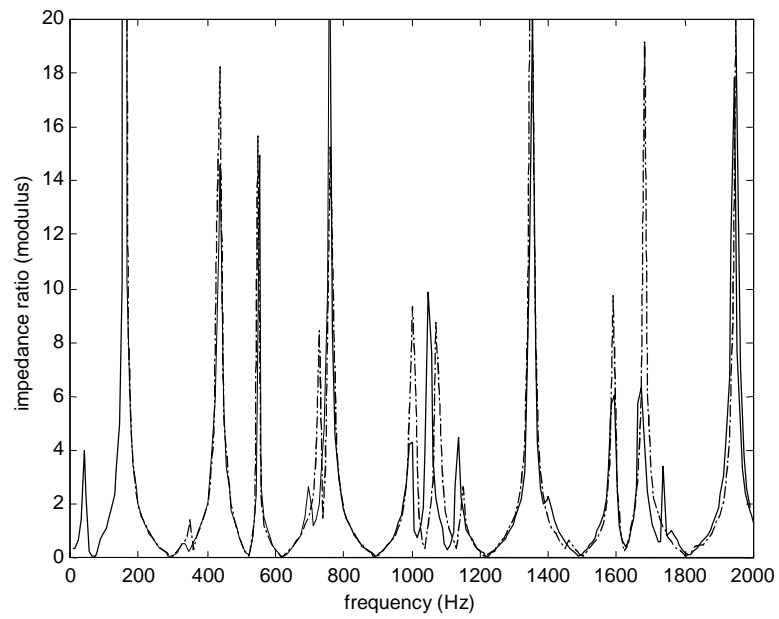


Figure: 9

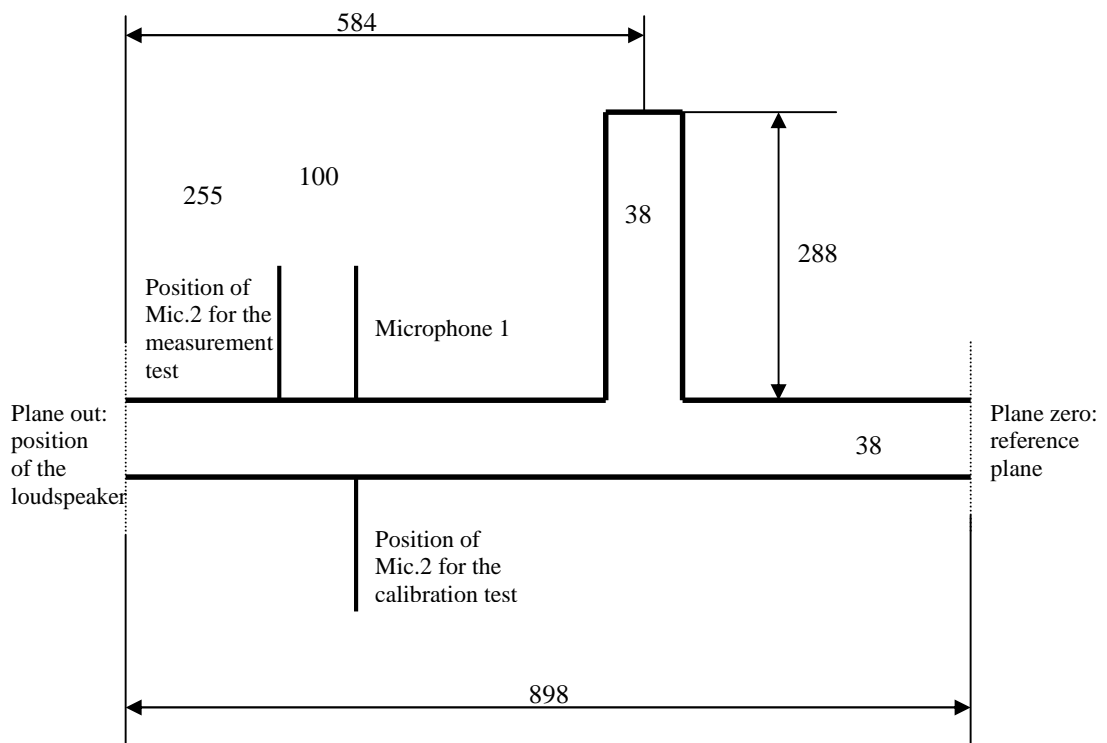


Figure: 10

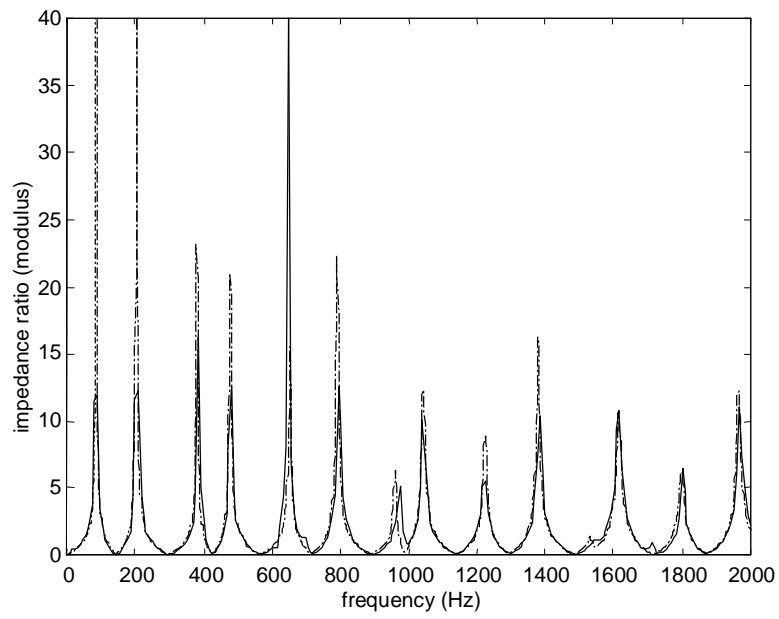


Figure: 11

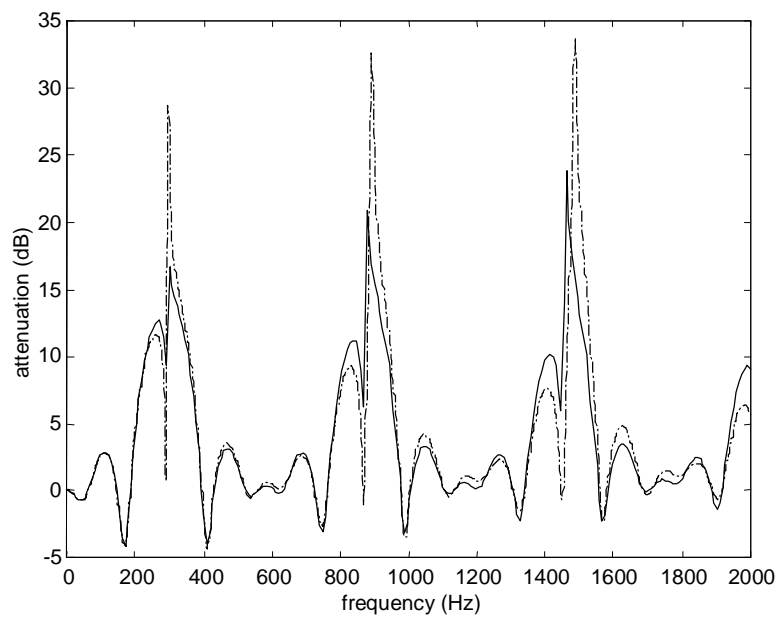


Figure: 12

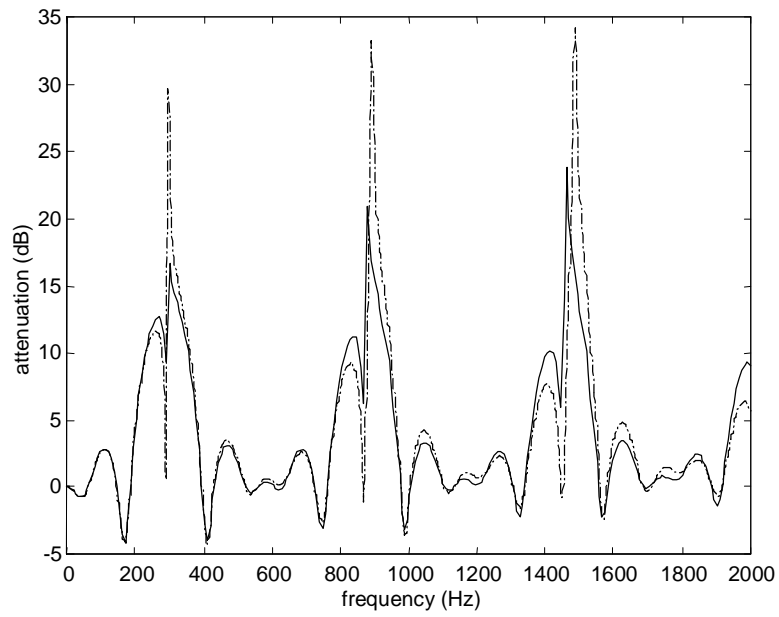


Figure: 13

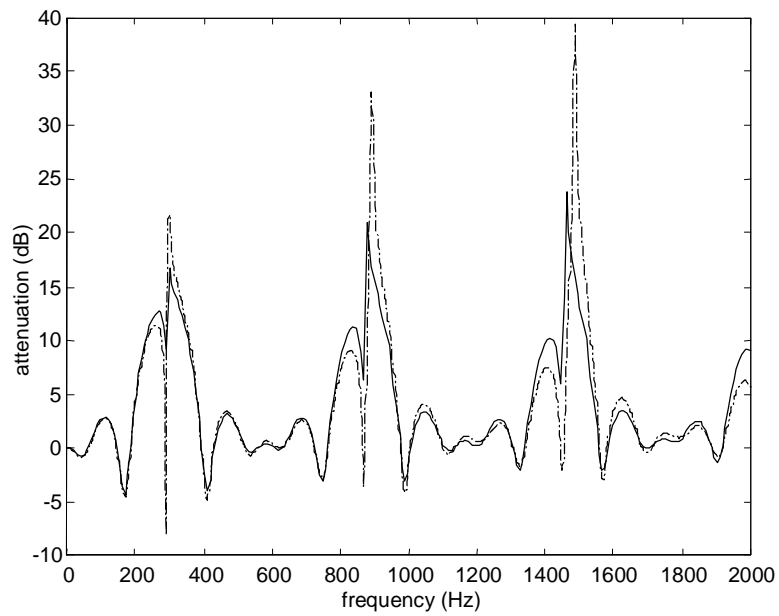


Figure: 14

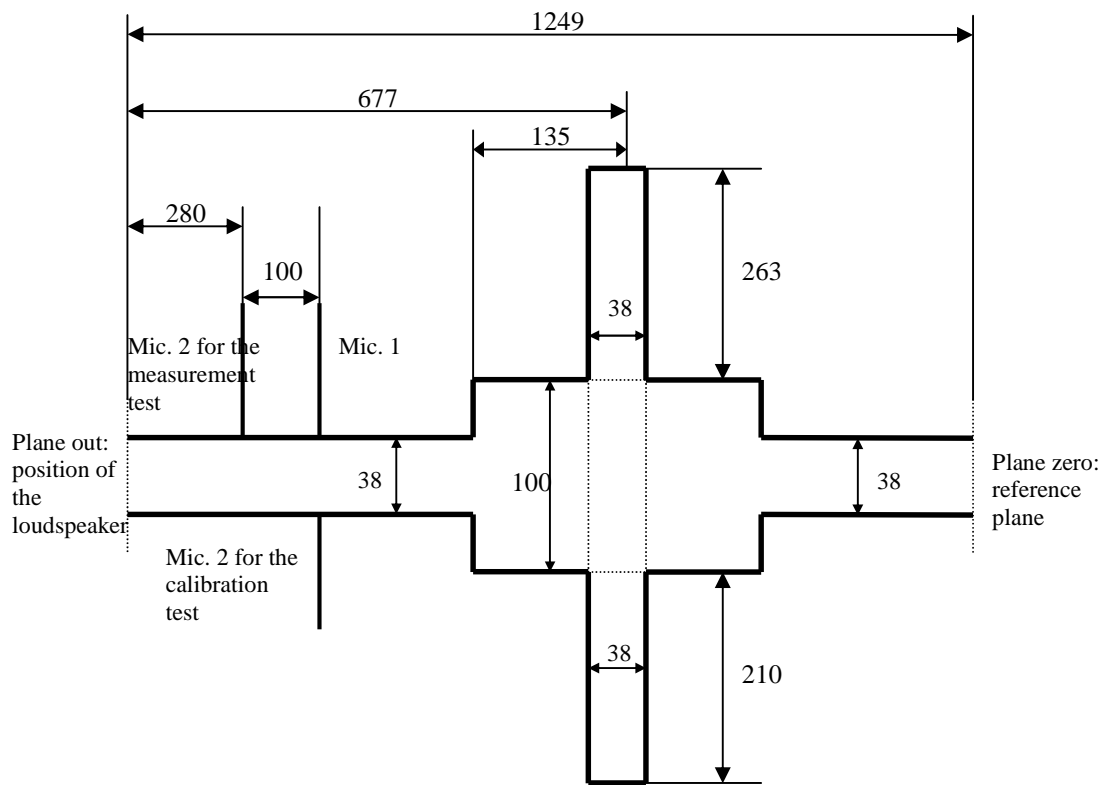


Figure: 15

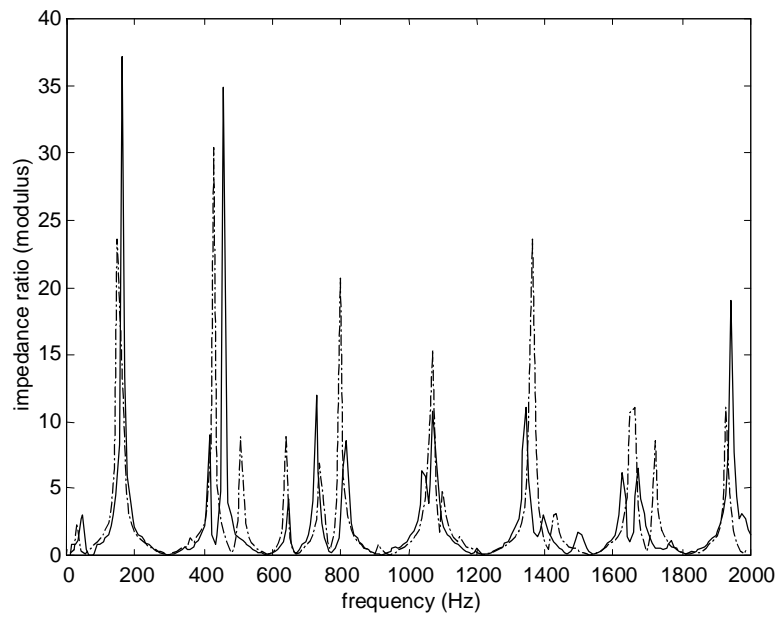


Figure: 16

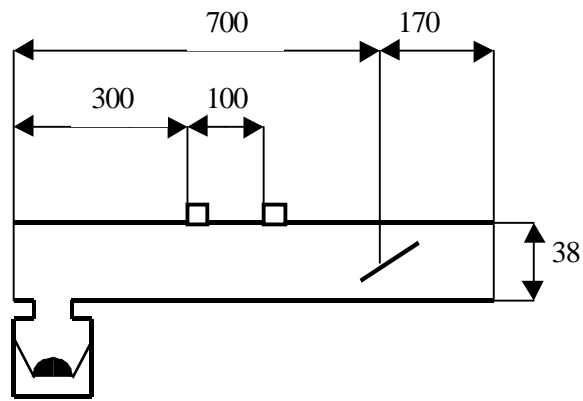


Figure: 17

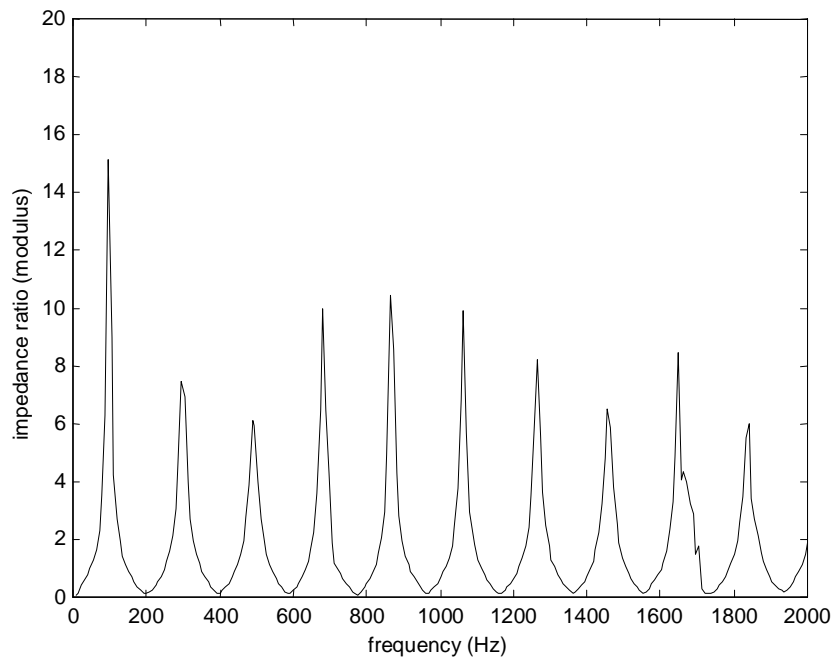


Figure: 18

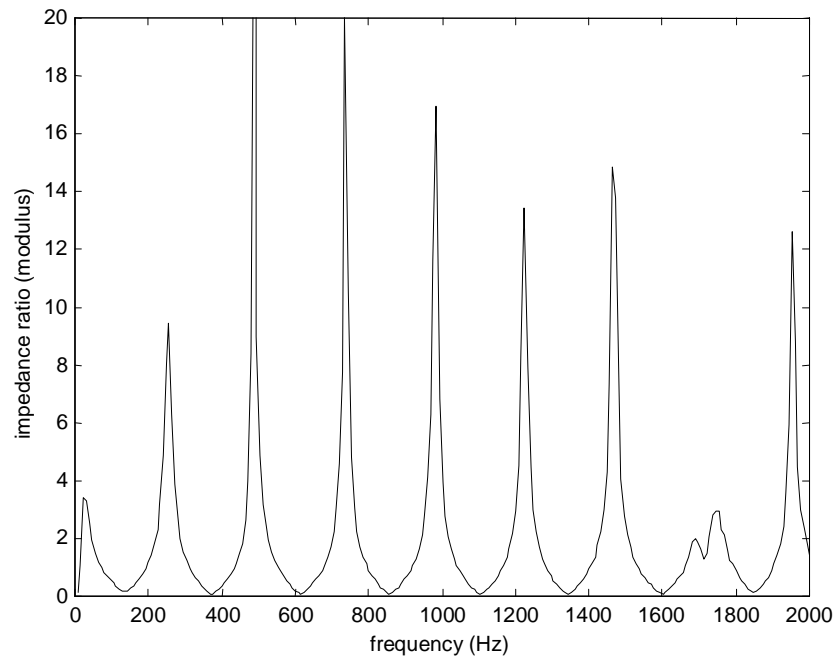


Figure: 19

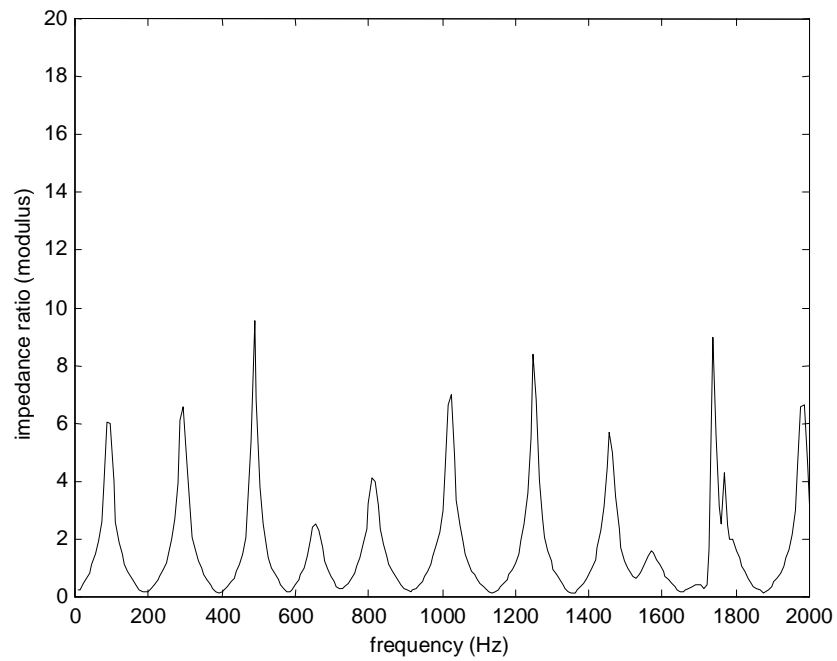


Figure: 20

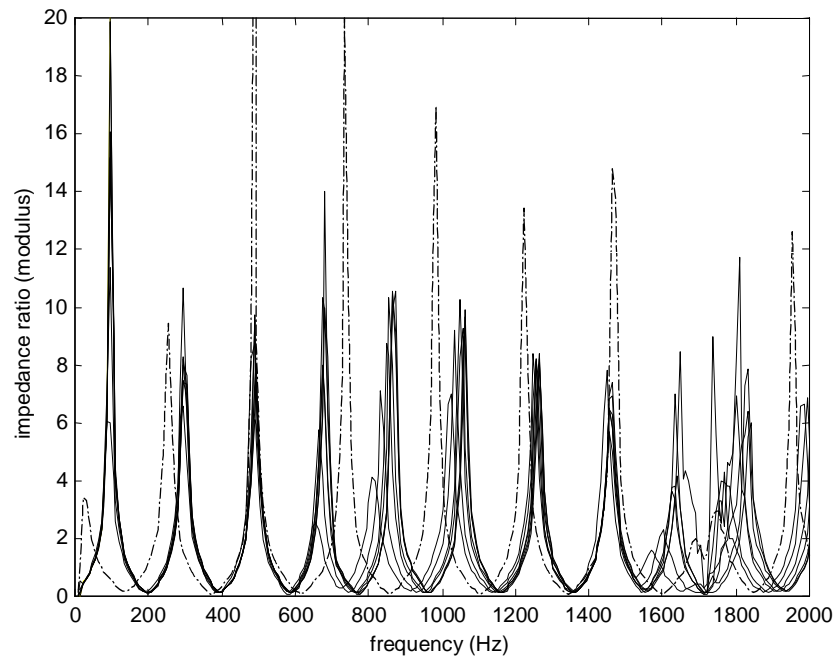


Figure: 21

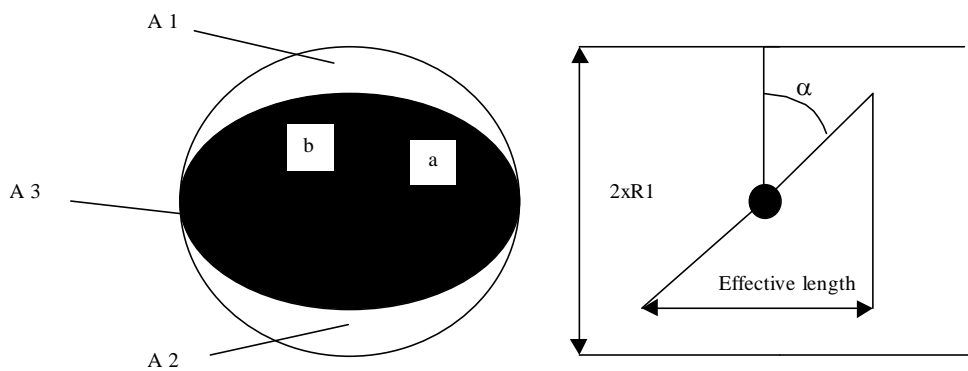


Figure: 22

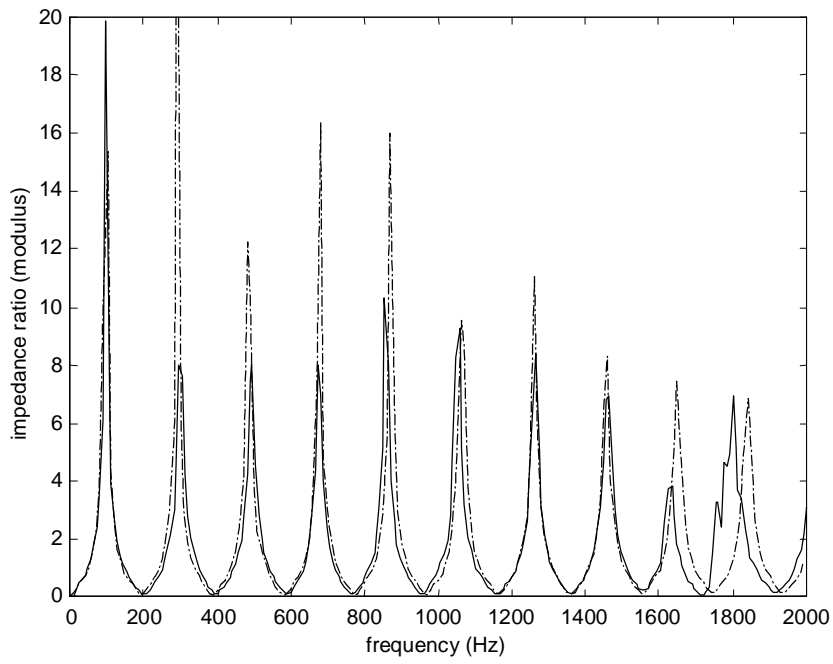


Figure: 23

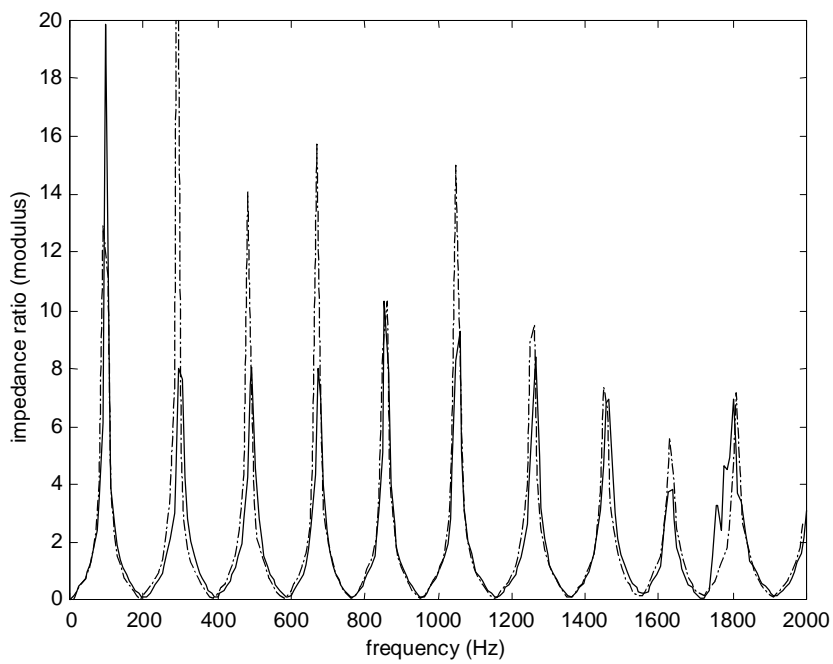


Figure: 24

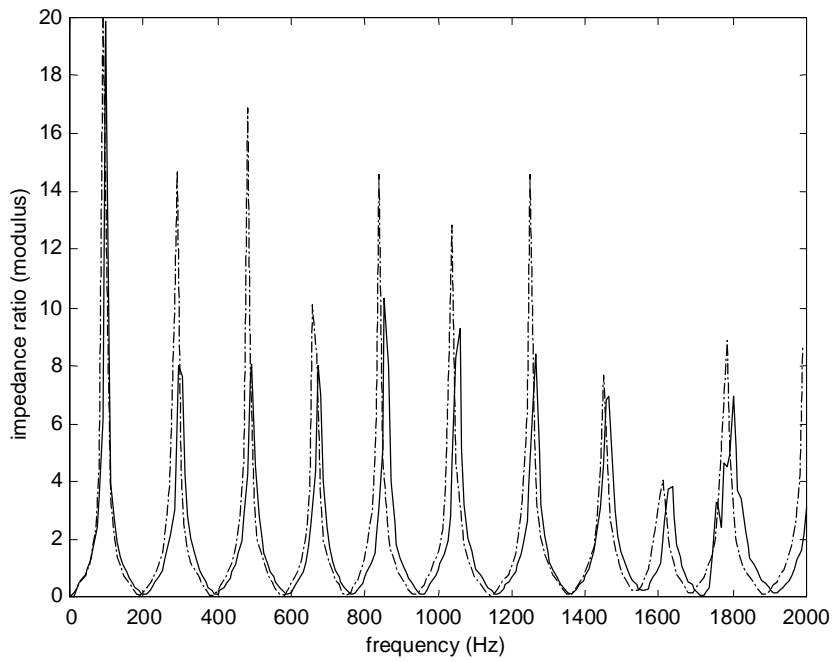


Figure: 25

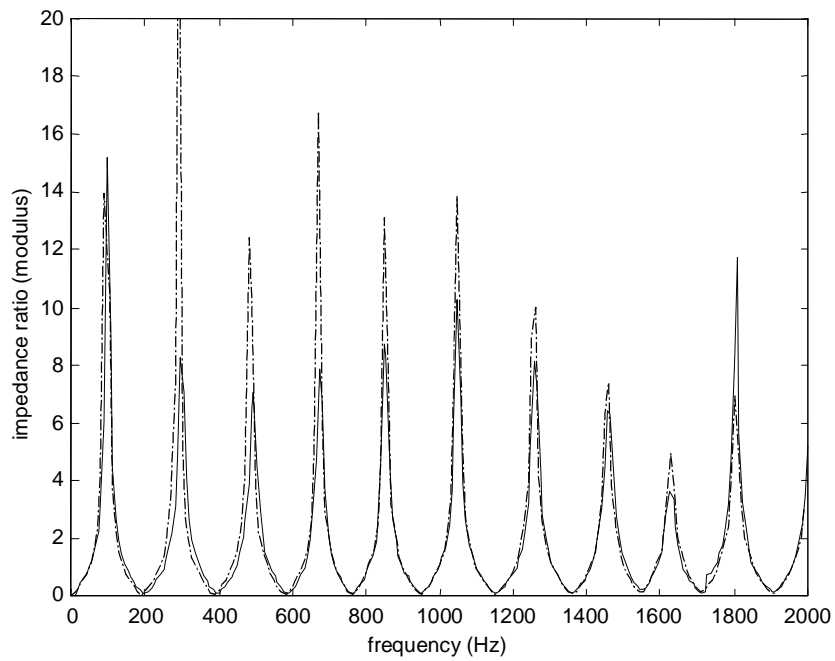


Figure: 26 Measured and calculated results for 30° open throttle, L3=3mm

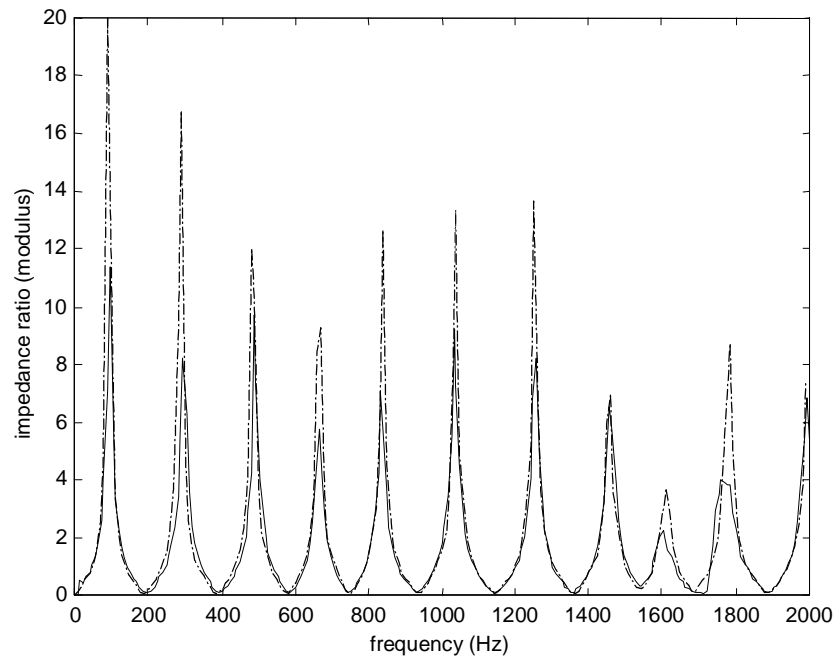


Figure: 27 Measured and calculated results for 15° open throttle, L3=1.3mm

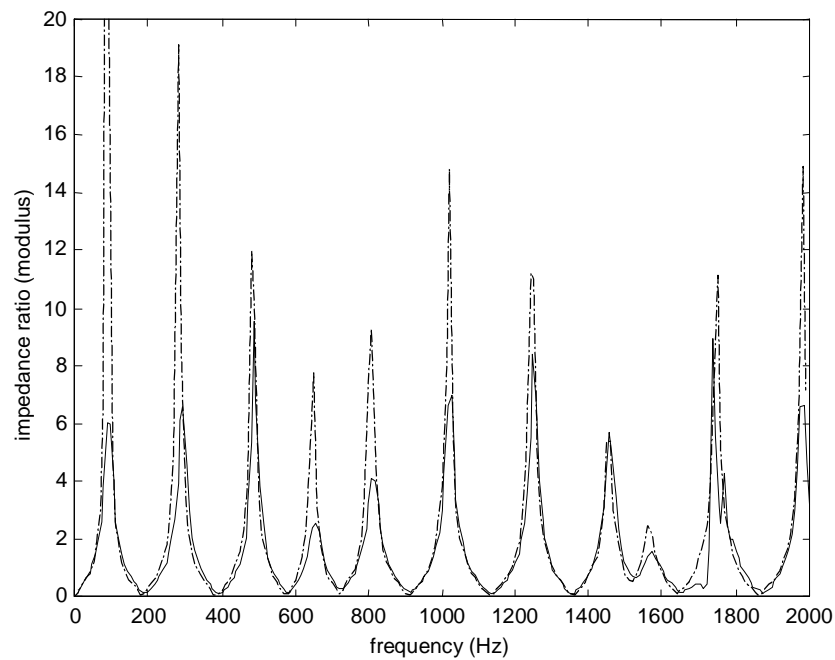


Figure: 28

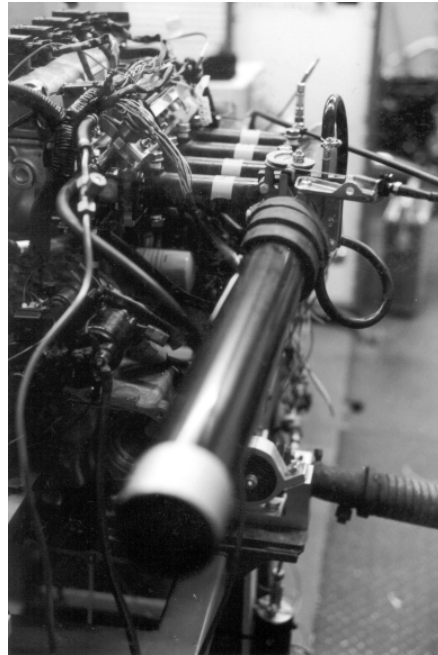


Figure: 29

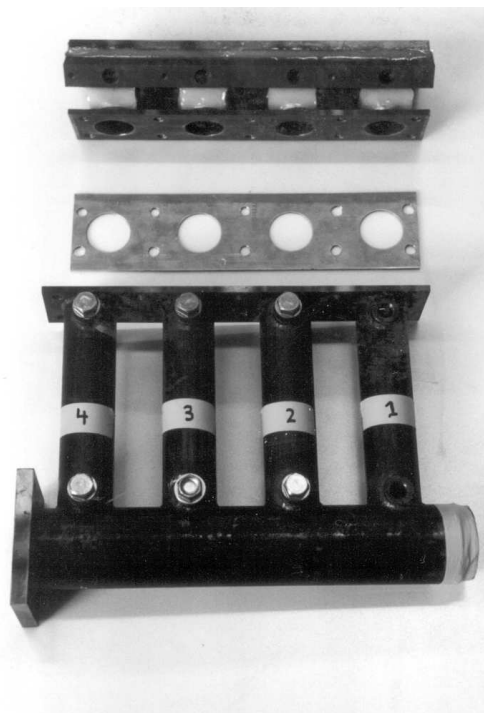


Figure: 30

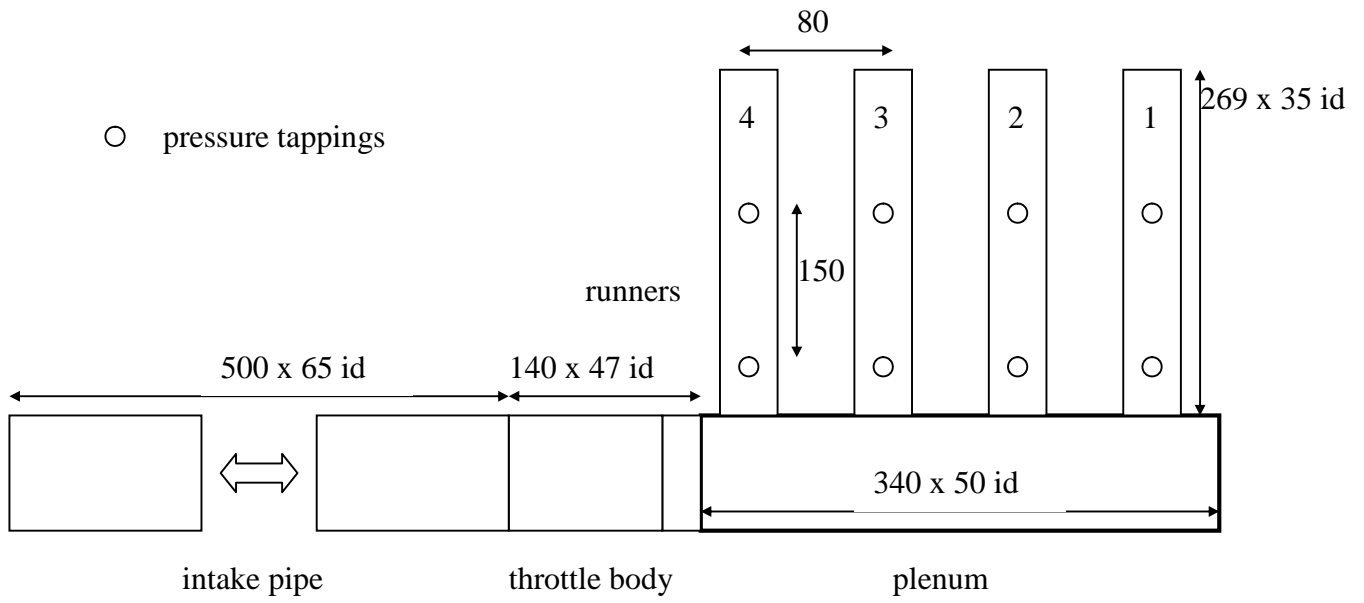


Figure: 31

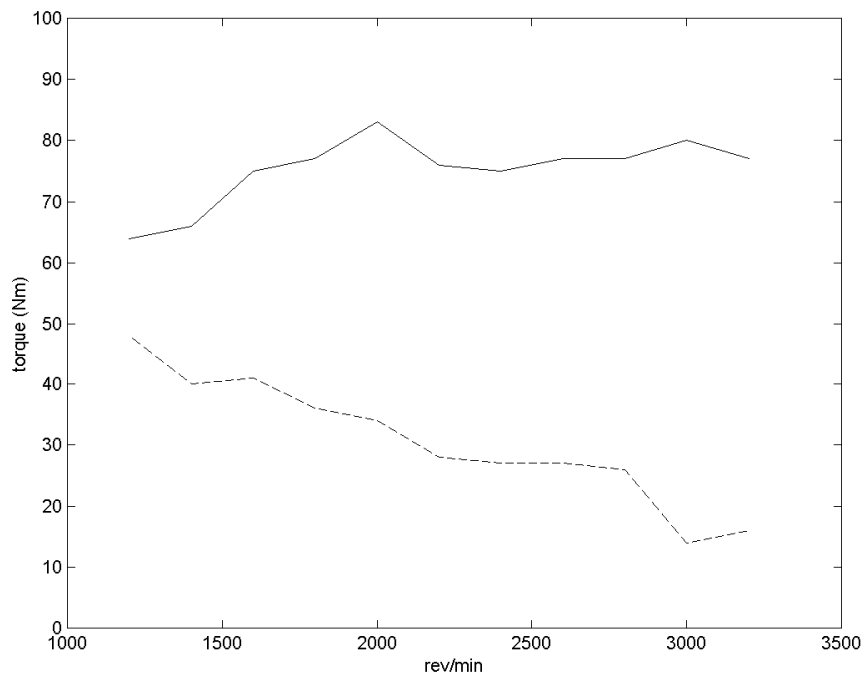


Figure: 32

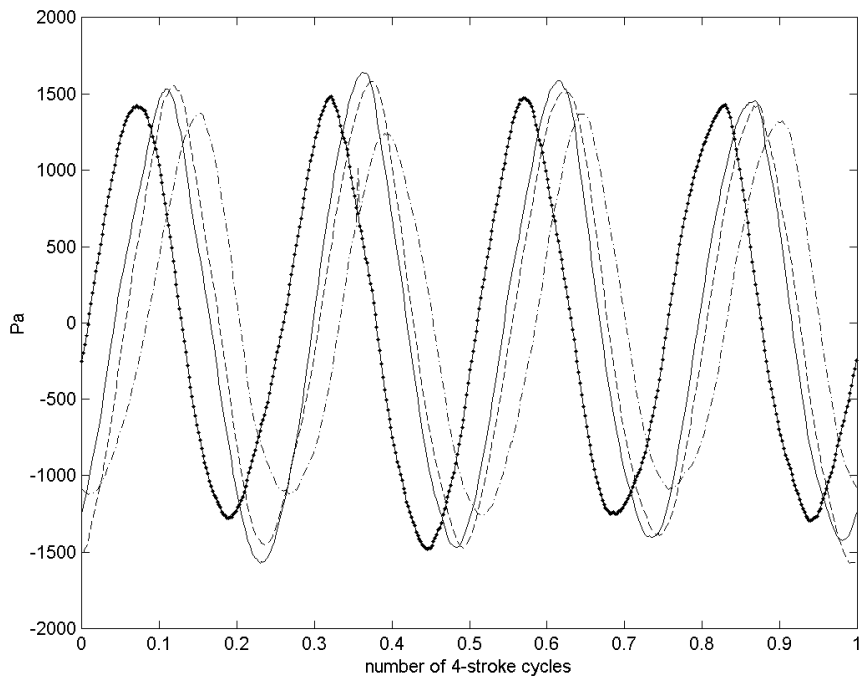


Figure: 33

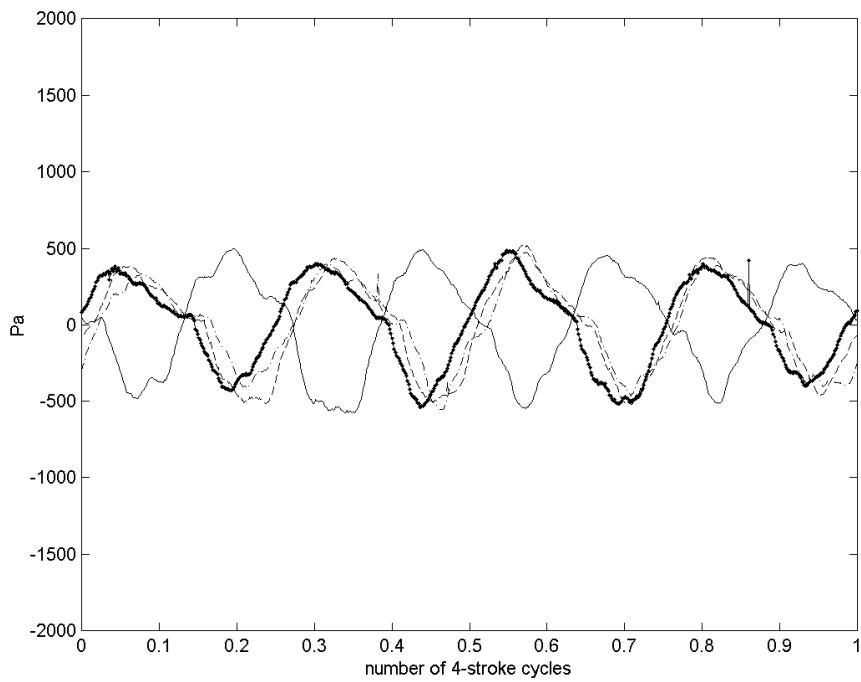


Figure: 34

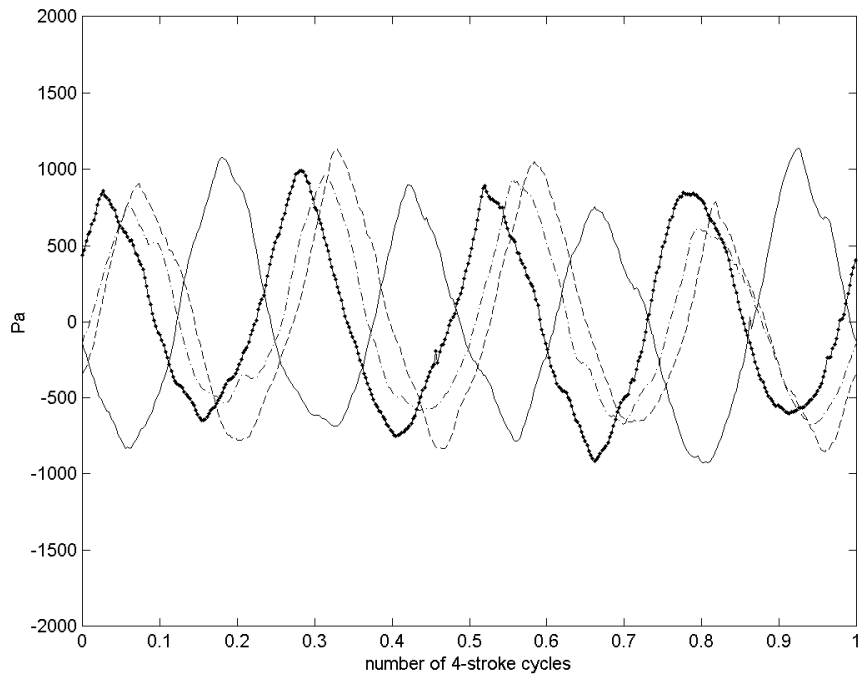


Figure: 35

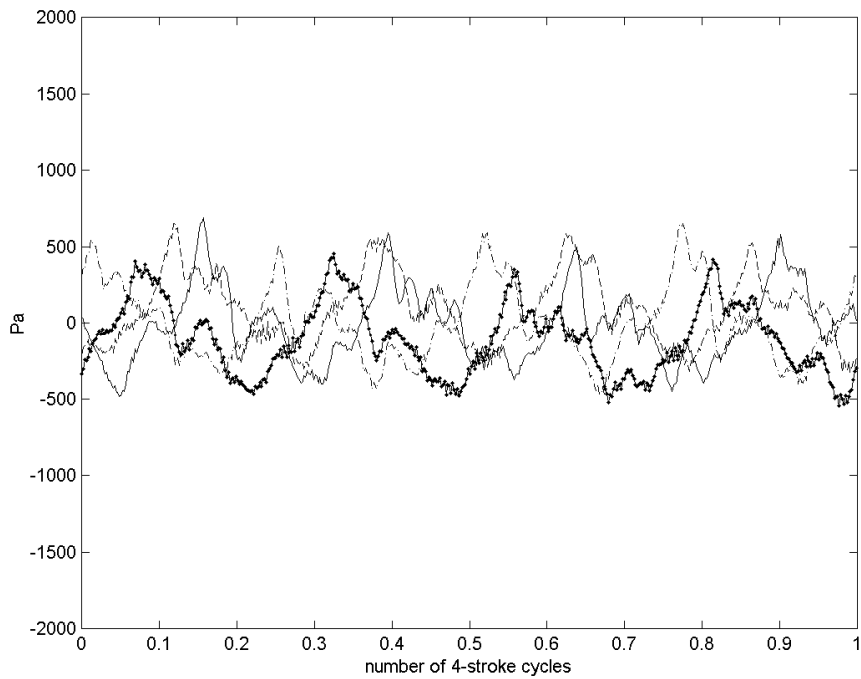


Figure: 36

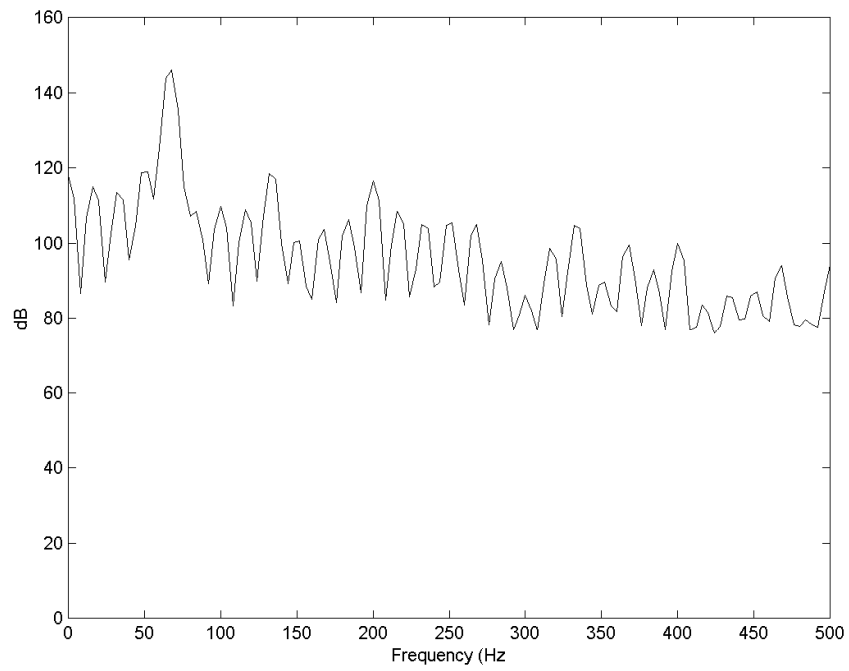


Figure: 37

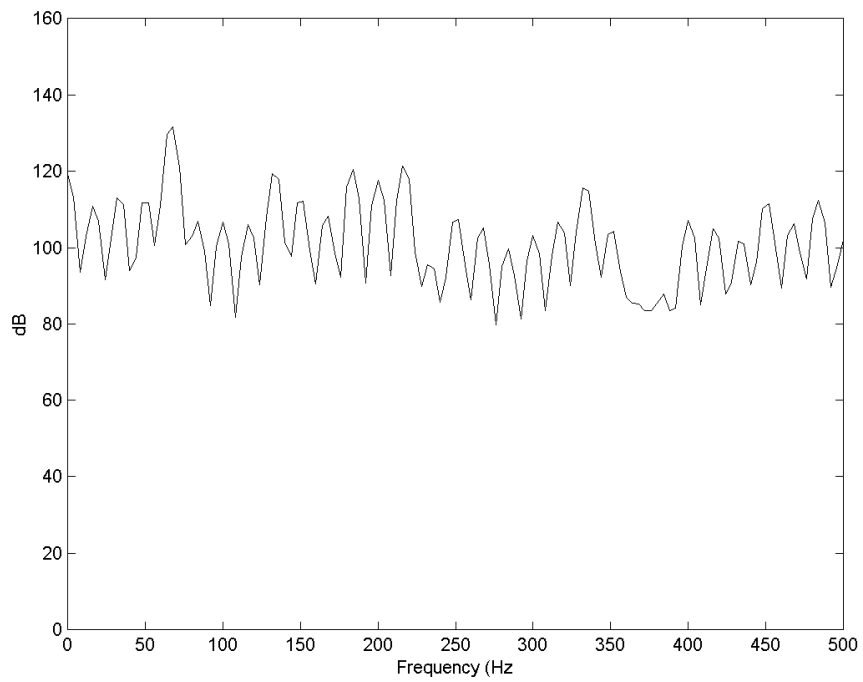


Figure: 38

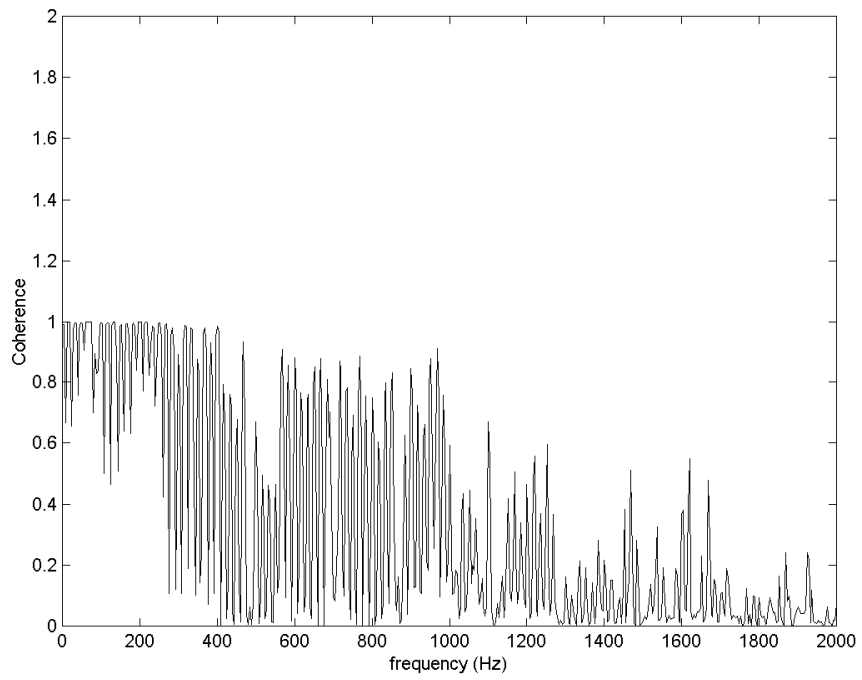


Figure: 39

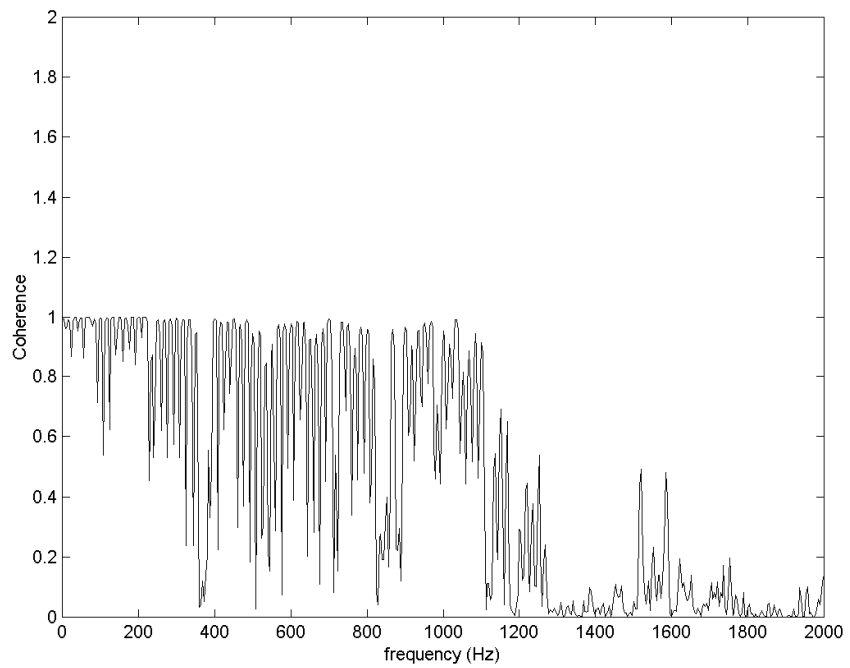


Figure: 40

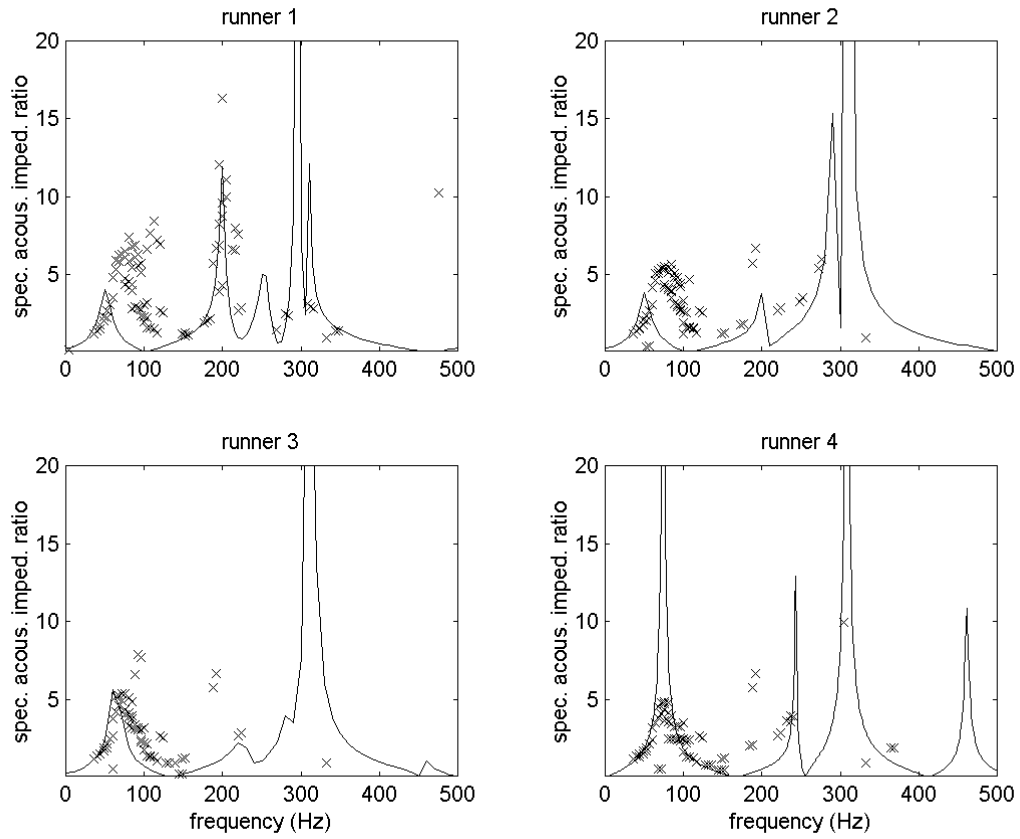


Figure: 41

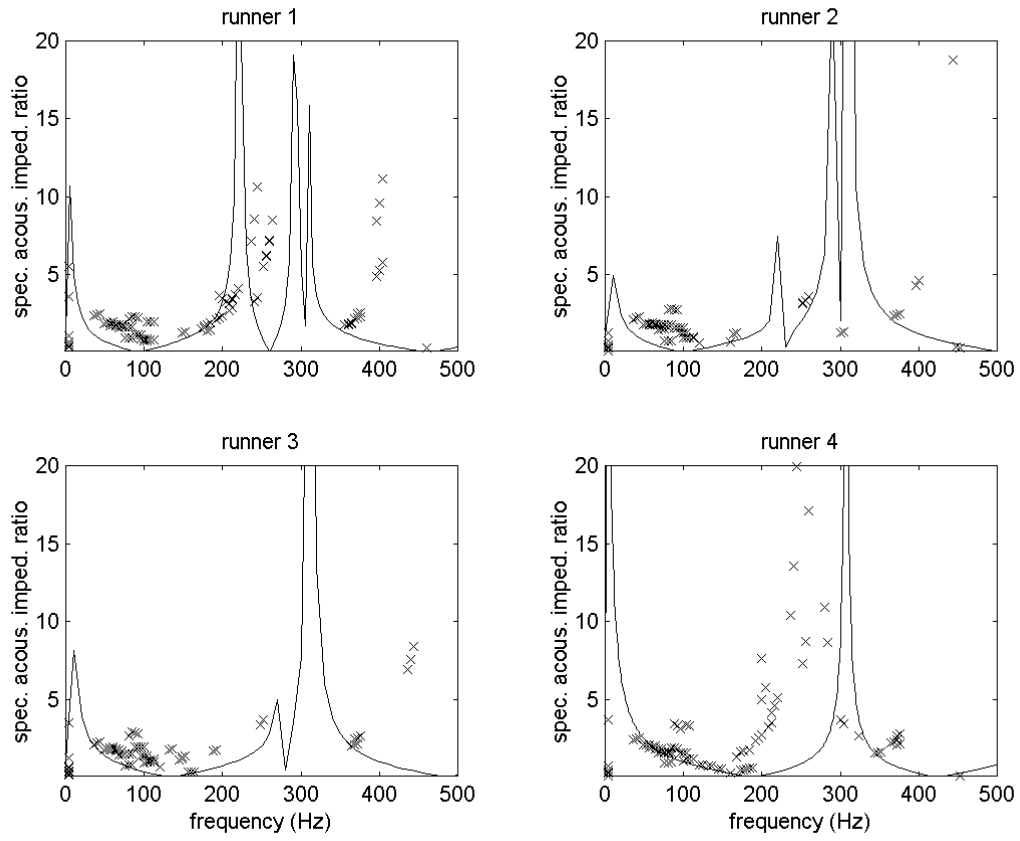


Figure: 42